

Lattice Boltzmann simulation of deformable fluid-filled bodies: progress and perspectives

Danilo P. F. Silva,^{1,2} Rodrigo C. V. Coelho,^{1,2} Ignacio Pagonabarraga,^{3,4} Sauro Succi,^{5,6} Margarida M. Telo da Gama,^{1,2} and Nuno A. M. Araújo^{1,2}

¹*Centro de Física Teórica e Computacional, Faculdade de Ciências, Universidade de Lisboa, P-1749-016 Lisboa, Portugal*

²*Departamento de Física, Faculdade de Ciências, Universidade de Lisboa, P-1749-016 Lisboa, Portugal*

³*Departament de Física de la Matèria Condensada, Universitat de Barcelona, Carrer de Martí Franquès 1, 08028 Barcelona, Spain*

⁴*Universitat de Barcelona Institute of Complex Systems (UBICS), Universitat de Barcelona, 08028 Barcelona, Spain*

⁵*Center for Life Nano Science at La Sapienza, Istituto Italiano di Tecnologia, 295 Viale Regina Elena, I/00161 Roma, Italy*

⁶*Harvard Institute for Applied Computational Science, Cambridge, MA 02138, USA*

(*Electronic mail: dpsilva@fc.ul.pt, rcvcoelho@fc.ul.pt)

(Dated: 13 December 2023)

With the rapid development of studies involving droplet microfluidics, drug delivery, cell detection, and microparticle synthesis, among others, many scientists have invested significant efforts to model the flow of these fluid-filled bodies. Motivated by the intricate coupling between hydrodynamics and the interactions of fluid-filled bodies, several methods have been developed. The objective of this review is to present a compact foundation of the methods used in the literature in the context of lattice Boltzmann methods. For hydrodynamics, we focus on the lattice-Boltzmann method due to its specific ability to treat time- and spatial-dependent boundary conditions and to incorporate new physical models in a computationally efficient way. We split the existing methods into two groups with regard to the interfacial boundary: *fluid-structure* and *fluid-fluid methods*. The fluid-structure methods are characterised by the coupling between fluid dynamics and mechanics of the flowing body, often used in applications involving membranes and similar flexible solid boundaries. We further divide fluid-structure-based methods into two subcategories, those which treat the fluid-structure boundary as a continuum medium and those that treat it as a discrete collection of individual springs and particles. Next, we discuss the fluid-fluid methods, particularly useful for the simulations of fluid-fluid interfaces. We focus on models for immiscible droplets and their interaction in a suspending fluid and describe benchmark tests to validate the models for fluid-filled bodies.

I. INTRODUCTION

The many-body dynamics of deformable objects, passive and active alike, in confined fluid flows is a central theme of modern soft matter research, with many applications in science, engineering, and medicine. From a fundamental perspective, the main challenge relates to the self-consistent interplay between external degrees of freedom, positions and momenta, and the internal ones describing the shape changes of the deformable body. Such an interplay is expected to spawn new dynamic regimes that are simply inaccessible to rigid particles. Likewise, such new dynamic regimes are expected to lead to new states of soft matter, hence potentially new materials.

In this review, we shall focus on the transport of deformable fluid-filled bodies, an important problem with various applications, from oil to pharmaceutical and food-processing industries¹⁻⁴. Familiar examples include paints, milk, and blood, where the internal constituents are ink droplets, fat droplets, and cells, respectively, and all deform when subjected to mechanical stresses, such as the ones resulting from the flow of the surrounding fluid. An analytical approach proves challenging due to the strong coupling between the fluid and the deformable particles. This interaction is reciprocal, for the

fluid affects the shape of the particle due to hydrodynamic forces and the deformation in turn changes the boundaries of the fluid flow. While still facing numerous challenges, computational methods have become an indispensable alternative tool to study these systems⁵⁻⁸.

Numerical models for the interplay between the macroscopic fluid properties and its internal deformable constituents usually combine computational fluid dynamics (CFD) with computational mechanics⁹⁻¹¹. This is particularly true for the simulation of fluid-filled bodies with solid boundaries. Deformability alters the flow, hence it affects the way energy is dissipated within the flow, resulting in strong rheological and mechanical nonlinearities, as signaled by the crossover from Newtonian to shear-thinning regimes, such as in most emulsions. A fluid-filled body consists of a body, usually spherical, with a fluid core (see Fig. 1). Common examples include droplets and capsules. The latter is a liquid droplet enclosed by a thin membrane. These bodies are often surrounded by a fluid environment and consequently, they exhibit fluid-fluid boundaries (droplets) or fluid-solid boundaries (capsules).

The modelling approaches for fluid-filled bodies can be divided into two groups, based on the boundary between the fluid-filled body and its environment. These are fluid-structure and fluid-fluid methods. The former consists of modelling a fluid-solid boundary, where the fluid and a deformable solid

interact with each other. The second consists of modelling the interactions between two fluids, usually separated by a fluid-fluid interface. The nature of the boundaries requires computational methods to describe both the fluid inside and outside of the particles. Furthermore, tracking the interface is often required, which can make the overall process computationally expensive. In this review, we focus on cases where the internal and external fluids are both Newtonian. We point out that for industrial applications, capsules can have solid cores (even multiple small solid cores) enclosed by a membrane; however this will not be addressed in this review¹².

Computational methods can often illuminate regions of parameter space not easily accessible by experiments or analytical methods. Several methods can be used to model the fluid flow. Here, we focus on the lattice Boltzmann method (LBM), as it provides a versatile way to introduce fluid-fluid interactions and to couple fluid-solid boundaries as well. Various methods (continuum, discrete, mesoscopic) have been developed to simulate droplets, cells, capsules and so on, and we refer to existing literature on this^{13,14}. We restrict ourselves to those methods that employ or pertain to LBM. Previous reviews and books^{15–17} have covered some fluid-solid and fluid-fluid methods in a different context. For instance, Karimnejad et. al.¹⁵ have reviewed fluid-structure (FS) methods for rigid particles. Here our focus is on methods for deformable particles in fluids. We present a comprehensive review of those methods and compare them.

Finally, we wish to underline that the methods described in this review straddle across the passive versus active soft matter divide, just because, once the coupling between internal and external degrees of freedom is accounted for, such divide largely blurs out¹⁸. The methods described here may be used to investigate problems in the active matter systems such as the emergent nematic order in epithelial cells, which share many similarities with the emulsions of Sec. IV, and the shape changes in bacteria, which become more elongated when swarming^{19,20}.

The review is organised as follows. The LBM is summarised in Sec. II. In Sec. III, we review fluid-structure methods which often use the immersed boundary method. We highlight the differences and similarities between the continuum and the discrete approaches. In Sec. IV, we review the various multicomponent methods for immiscible droplets. In Sec. V, we provide benchmarks in 2D and 3D for hydrostatic and hydrodynamic conditions. In Sec. VI, we conclude by summarising our observations and make remarks on open questions and future challenges.

II. LATTICE BOLTZMANN METHOD

In recent years the LBM has become a useful tool in solving the hydrodynamics of soft matter systems²¹. The fluid flow is described by the Navier-Stokes (NS) equations,

$$\rho \left(\frac{\partial \mathbf{u}}{\partial t} + (\mathbf{u} \cdot \nabla) \mathbf{u} \right) = -\nabla p + \mu \nabla^2 \mathbf{u} + \mathbf{g}, \quad (1)$$

$$\nabla \cdot \mathbf{u} = 0,$$

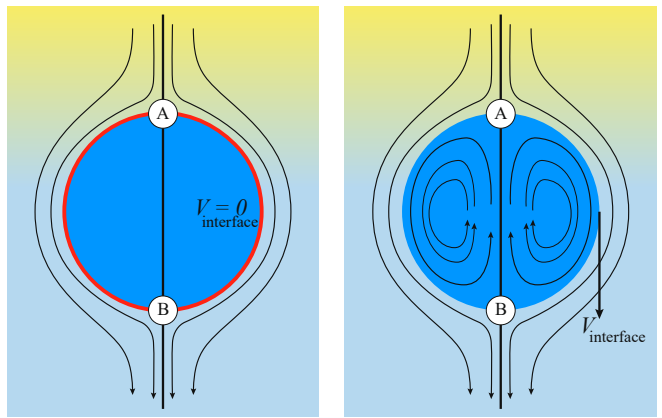


FIG. 1. Comparison of flow around a fluid-solid (left) and a fluid-fluid (right) interface. On the left, the red line represents a fluid-solid interface such as a membrane on a rigid capsule. There is no internal circulation because the velocity at the interface is zero (considering no-slip boundary conditions). On the right, we see internal circulation due to the continuity of the velocity across the fluid-fluid interface. Points A and B indicate stagnation points and the colour gradient of the external fluid represents a pressure gradient which drives the flow. Both images are in the capsule reference frame (fluid velocity relative to the capsule/droplet). The internal fluid in both images is blue. Black arrows represent the fluid flow.

where \mathbf{u} is the fluid velocity, t is time, p is the pressure field, μ is the dynamic viscosity, ρ is the density and \mathbf{g} is the body force. LBM however does not solve the NSE directly. Instead, it is a mesoscopic method which recovers the results of the Navier-Stokes equations. As opposed to molecular dynamics, which solves the dynamics of individual molecules/atoms, in LBM a fluid “particle” consists of a group of molecules and consequently is much larger than the individual scale of molecules. Information about the fluid is contained in the lattice nodes and can only move in specific directions reducing the number of degrees of freedom. Although it originates from Lattice Gas Automata²², it is now considered a separate method. Several works have shown the potential of LBM to solve fluid-related problems^{5,23–27}. It is an efficient algorithm particularly popular for Stokes flow, systems with complex solid boundaries²⁸, multiphase flow²⁹, hydrodynamic dispersion³⁰ and convection³¹.

A. Lattice BGK model

The Boltzmann equation that contains the fluid particle information reads

$$\frac{\partial f}{\partial t} + \mathbf{v} \cdot \nabla f + \mathbf{a} \cdot \nabla_{\mathbf{v}} f = \Omega(f) \quad (2)$$

where $f = f(\mathbf{x}, \mathbf{v}, t)$ is the distribution function for a fluid particle in phase space, having microscopic velocity, \mathbf{v} , at time t , at position \mathbf{x} , where \mathbf{a} is the acceleration and $\Omega(f)$ is the collision operator which describes the interaction between molecules. Different LBM formulations will have different

collision operators. The simplest one is the Bhatnagar-Gross-Krook (BGK) operator given by

$$\Omega(h) = -\frac{f(\mathbf{x}, \mathbf{v}, t) - f^{eq}(\mathbf{x}, \mathbf{v}, t)}{\tau}, \quad (3)$$

where τ is the relaxation time which drives the relaxation to the equilibrium distribution $f^{eq}(\mathbf{x}, \mathbf{v}, t)$. The relaxation time is directly related to the viscosity of the fluid since the fluid kinematic viscosity ν is related to the single relaxation time τ by

$$\nu = c_s^2 \left(\tau - \frac{\Delta t}{2} \right), \quad (4)$$

where c_s is the speed of sound and Δt is the time step. It should be stated, however, that connecting the kinematic viscosity and the speed of sound is shown to be valid for low Mach number (< 0.3) and nearly incompressible flow.

The equilibrium distribution function is related to the macroscopic fluid velocity \mathbf{u} and density ρ

$$f^{eq} = \frac{\rho}{(2\pi\theta)^{D/2}} \exp \left[-\frac{(\mathbf{v} - \mathbf{u})^2}{2\theta} \right], \quad (5)$$

where θ is the normalised temperature which is usually unity and D is the spatial dimension. The above equation can be expanded using the Hermite series to the second order as

$$f_\alpha^{eq}(\mathbf{x}_i, t) = w_\alpha \rho \left(1 + \frac{\boldsymbol{\xi}_\alpha \cdot \mathbf{u}}{c_s^2} + \frac{(\boldsymbol{\xi}_\alpha \cdot \mathbf{u})^2}{2c_s^4} - \frac{\mathbf{u}^2}{2c_s^2} \right), \quad (6)$$

where α is the index of discretized velocities, $\boldsymbol{\xi}_\alpha$ is the microscopic velocity vector, i is the index of lattice sites, and w_α is the weight of the lattice. $f_\alpha^{eq}(\mathbf{x}_i, t)$ is the distribution at equilibrium at position \mathbf{x}_i and time t . Both ρ and \mathbf{u} are a function of position \mathbf{x}_i and time t . The parameters $\boldsymbol{\xi}_\alpha$ and w_α depend on the lattice chosen for the discretization. The velocity is discretized into structured lattice velocity (1D, 2D or 3D) vectors. For example, the D1Q3 lattice represents a one-dimensional chain with three vectors per node. Usually, more lattice vectors mean increased precision but also increased computational effort. Popular lattices include the D2Q9 (see Fig. 2) and D3Q19. Different lattices have different speeds of sound c_s and weights w_α for each vector³².

The final discrete lattice Boltzmann equation (with the BGK operator) is,

$$\underbrace{f_\alpha(\mathbf{x}_i + \boldsymbol{\xi}_\alpha \Delta t, t + \Delta t)}_{\text{streaming}} = \underbrace{f_\alpha(\mathbf{x}_i, t) - \frac{\Delta t}{\tau} [f_\alpha(\mathbf{x}_i, t) - f_\alpha^{eq}(\mathbf{x}_i, t)] + \mathcal{F}_\alpha \Delta t}_{\text{collision}}, \quad (7)$$

where \mathcal{F}_α is the forcing term which includes both external forces and intra/intermolecular fluid forces. There are two main steps in Eq. 7: collision and streaming (see Fig. 2). The information for both steps comes from the neighbours of

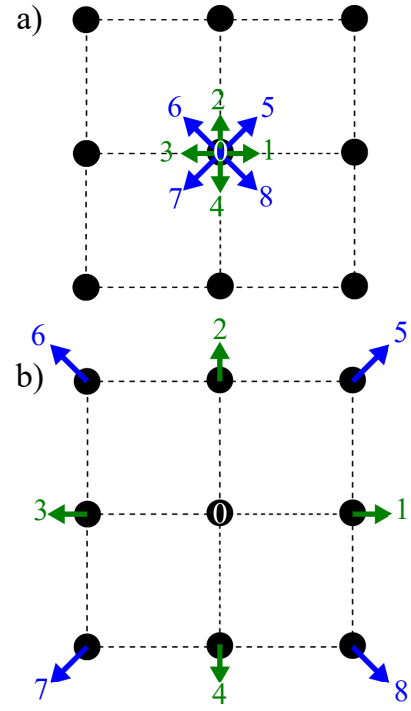


FIG. 2. Two main steps of the LBM: (a) collision and (b) streaming using a D2Q9 lattice. The collision is described by the distribution functions going from one node after the streaming step propagates them to the neighbouring nodes according to the direction. The arrows represent the nine distribution functions.

the respective fluid node. This makes parallelization easier in clusters of computers or on graphical processing units (GPU) compared to other conventional methods.

The macroscopic density and velocity are calculated through

$$\begin{aligned} \rho(\mathbf{x}, t) &= \sum_{\alpha} f_{\alpha}(\mathbf{x}, t), \\ \rho \mathbf{u}(\mathbf{x}, t) &= \sum_{\alpha} \boldsymbol{\xi}_{\alpha} f_{\alpha}(\mathbf{x}, t). \end{aligned} \quad (8)$$

There are different force schemes in LBM used to implement these terms. Several articles and reviews have been written about the advantages/disadvantages of each one (see Refs.^{33–35}). A popular one, the Guo forcing scheme³⁶, is given by

$$\mathcal{F}_\alpha \Delta t = \left(1 - \frac{1}{2\tau} \right) w_\alpha \left[\frac{\boldsymbol{\xi}_\alpha \cdot \mathbf{u}}{c_s^2} + \frac{(\boldsymbol{\xi}_\alpha \cdot \mathbf{u}) \boldsymbol{\xi}_\alpha}{c_s^4} \right] \cdot \mathbf{F}, \quad (9)$$

where \mathbf{F} is the force.

In this review, we focus on the lattice Boltzmann method to model the hydrodynamics. The LBM is particularly well suited to multiphase flow, particularly drops, bubbles, and emulsions. Some of the commonly quoted strengths and weaknesses of the LBM method are discussed, for example, in Refs.^{32,37}.

III. FLUID-STRUCTURE BASED METHODS

At the microscale, there is a plethora of particles which are bound by membranes. Examples include living cells, artificial capsules (e.g. polymerised membranes) and vesicles (e.g. lipid bilayer membranes). An example of biological membrane-bound particles is red blood cells (RBCs). We highlight that variations of the models presented here have been used for soft objects like microgels³⁸ and capsules³⁹. While these bodies can suffer strong deformations, for the majority of them, volume and surface area are relatively unchanged. Thus, it is no surprise that the transport of complex fluids (e.g. blood) has been the focus of both biomedical and mechanical research for many decades. To capture the realistic mechanical and rheological characteristics of both biological and synthetic membrane-bound particles, mechanical models should have the capability to consider membrane elastic and viscous properties, bending resistance, and the viscosity of the external and internal fluids. In modelling, the membrane is usually discretized into a mesh consisting of many individual line segments that are connected by nodes. In general, there are two ways to approach this problem. These approaches depend on whether the boundary (in most cases a membrane) is treated as a continuum medium or as a discrete one. We show in Fig. 3 an illustration of the two different approaches.

The first approach is a continuum one where the membrane is treated as a 2D continuum surface in 3D space. One simulates the solid mechanics of the membrane using appropriate constitutive laws that are descriptions of the energy-strain or stress-strain relations of the membrane. It is then possible to model strain-softening membranes, i.e. the membrane stress increases slower than strain, or strain-hardening membranes, where the membrane stress increases faster than strain⁴⁰. Although constitutive laws are rigorous physical descriptions of the membrane, the numerical implementation is complicated. In addition, due to the continuity of the membrane properties, this approach is limited to modelling at length scales where local differences in the membrane are insignificant⁴¹. Another consequence of applying a constitutive model in the entire membrane domain is that the shape memory might be neglected in some cases⁴². This approach is discussed in subsection III A.

In the second approach, the membrane is treated as a discrete network of springs and particles. This approach provides some advantages namely, its mathematical description is simpler and local differences or thermal fluctuations can be included in contrast to the continuum approach. However, spring constants can depend strongly on the mesh configuration as shown in Ref.⁴³. In fact, Ref.⁴³ shows that discrete spring models have anisotropic mechanical properties, in general. Furthermore, when studying biological membranes, local area incompressibility has to be enforced which is not possible using simple discrete spring models⁴³. Additional terms have to be included. This approach is also known to suffer less numerical instability than the continuum approach⁴¹. This discrete approach is discussed in subsection III B.

The elastic forces are treated differently in each approach.

In the continuum approach, these are solved using continuum-based solvers such as the finite element method (FEM) while in the discrete approach, the motion and interaction of individual springs are treated in a particle-based manner. Each approach has its own advantages and drawbacks which we highlight in the following sections. Additionally, the fluid can be coupled with membrane dynamics using the immersed boundary method. In subsection III C, we discuss how to couple the fluid mesh with the membrane mesh. This review focuses on LBM for the fluid which has a Cartesian fixed mesh and for the membrane a (triangular) evolving mesh. The immersed boundary method (IBM) has proven to be useful for partitioned simulations, where the flow and the displacement of the structure are calculated separately⁴⁴ and where the elastic bodies have negligible mass⁴⁵. In IBM, the flow is solved on an Eulerian grid while the membrane is treated on a Lagrangian grid⁴⁶. The total force acting on the membrane is treated as a source term in the NS equation. This means that artificial forces are spread as body forces around the membrane boundary in order to mimic the effects of the moving membrane. In the LBM, this is included in the \mathbf{g} term of Eq. (1), which ensures no slip and no flow penetration boundaries. Because the IBM is often employed for structures with negligible inertia (overdamped regime), the velocity of a membrane node is interpolated from the surrounding fluid while the forces acting on the membrane node are spread in the surrounding fluid nodes. IBM is discussed in more detail in subsection III C.

Once we define the constitutive models and constraints, it is straightforward to derive the nodal forces as will be shown. However, it is nontrivial to implement the force calculations. We give a summary of the nodal force calculation process. A membrane mesh is needed in both the continuum and discrete approaches. The vast majority of meshes used in the literature are triangular meshes. We aim, in the following subsections, to describe approaches to obtain those forces for elastic, immersed bodies. We illustrate different possible shapes with the fluid-structure-based models in Fig. 6.

A. Continuum approach

The membrane can be treated as a continuum sheet with infinitesimal thickness. The total energy of a membrane is

$$W = W_s + W_b + W_A + W_V, \quad (10)$$

where W_s is the elastic strain (in-plane) energy, W_b is the bending energy, W_A is the area penalty energy, and W_V is the volume penalty energy. We highlight that W_s is described by a continuum function which describes the in-plane energy. It is possible then to calculate elastic in-plane forces from W_s using FEM. Moreover, explicit expressions can be used for the calculation of bending and area/volume penalty forces as this does not necessarily require the FEM. In general, to solve the physics of the continuum membrane we need to discretize it using an appropriate mesh (usually triangular). The elementary surfaces in the mesh are connected by nodes which interact with the fluid. The force acting on membrane node i at

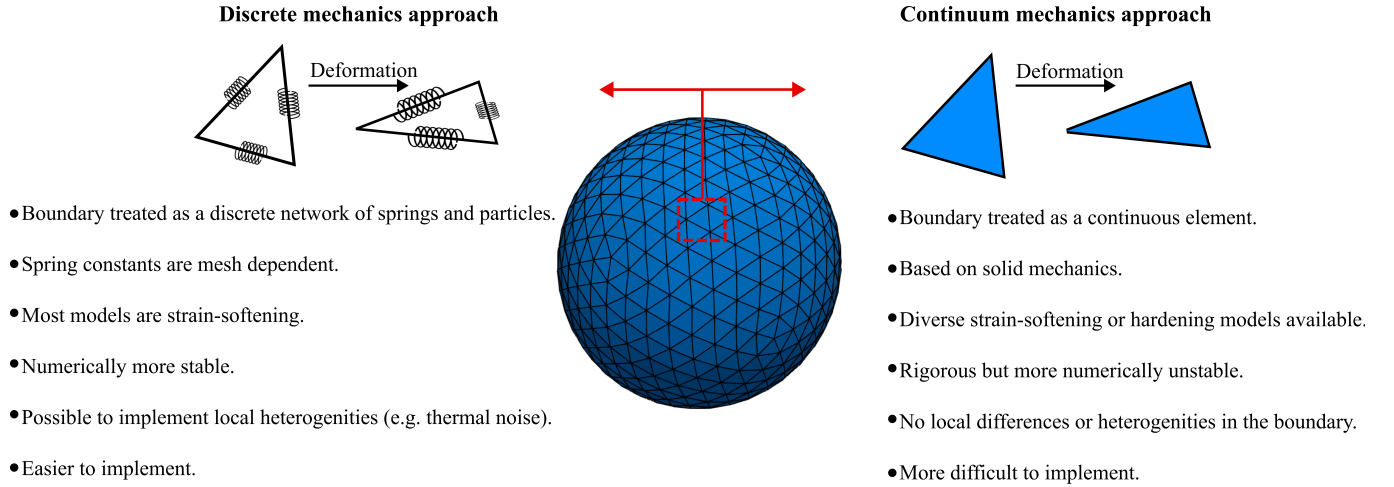


FIG. 3. Discrete mechanics approach (left) vs continuum mechanics approach (right). On the discrete mechanics approach the dynamics of the membrane is given by a connected network of springs. On the continuum mechanics approach the membrane is treated as a surface i.e. a continuum medium. The advantages and disadvantages of each approach are highlighted.

position x_i is given by the principle of virtual work^{47,48},

$$F_i = -\frac{\partial W}{\partial x_i}. \quad (11)$$

Details about derivations using the equation for each term can be found in Ref.⁴⁹. For simplicity, we usually consider more straightforward expressions for the force instead of the full expressions derived in the next sections.

1. Elastic membrane models and finite element method

In order to compute the elastic forces on membrane nodes, an appropriate constitutive equation, which describes the membrane properties is required. Among different constitutive equations, the Neo-Hookean (NH) law⁵⁰ is the simplest one with the strain energy function in the form

$$W_s^{\text{NH}} = \int_A \frac{E_s}{6} \left(\lambda_1^2 + \lambda_2^2 - 3 + \frac{1}{\lambda_1^2 \lambda_2^2} \right) dA, \quad (12)$$

where E_s is the surface shear elasticity modulus, λ_1 and λ_2 are the principle stretch ratios (see Fig. 4a) and dA is a surface element area. The NH constitutive equation models the membrane as a volume incompressible isotropic material which means that any increase in the area of the membrane due to its deformation is accompanied by thinning of the membrane thickness to preserve the membrane volume. Another version of NH law is the Zero-Thickness (ZT) shell formulation⁵¹. Here, a strain energy function is expressed as:

$$W_s^{\text{ZT}} = \int_A \frac{E_s}{6} \left[\lambda_1^2 + \lambda_2^2 - 2 - \log(\lambda_1^2 \lambda_2^2) + \frac{1}{2} \log^2(\lambda_1^2 \lambda_2^2) \right] dA. \quad (13)$$

The most popular model for red blood cell membrane was proposed by Skalak⁵² and then widely used; see e.g. Ref.^{10,53}.

The membrane is modelled as a 2D elastic sheet motivated by the small thickness of the membrane compared to its total surface area. This is useful to model membrane behaviour both for small stress loading and large deformations. In this model, the strain energy density function is defined as

$$W_s^{\text{SK}} = \int_A \frac{E_s}{12} \left[(\lambda_1^4 + \lambda_2^4 - 2\lambda_1^2 - 2\lambda_2^2 + 2) + C(\lambda_1^2 \lambda_2^2 - 1)^2 \right] dA, \quad (14)$$

where E_s and C are the membrane elastic shear and area dilation moduli. The same is true for other elastic models. Equations (12), (13), and (14) can also be written as a function of the strain invariants I_1 and I_2 defined for a 2D membrane (with isotropic and homogeneous properties) as

$$\begin{aligned} I_1 &= \lambda_1^2 + \lambda_2^2 - 2, \\ I_2 &= \lambda_1^2 \lambda_2^2 - 1. \end{aligned} \quad (15)$$

Once the constitutive law is chosen, we can compute the elastic forces using the linear finite element method⁴⁷. The elastic forces are computed at the Lagrangian nodes of the capsule mesh, using a linear finite element method that has been used in a number of capsule deformation models^{4,10,54}. The elastic forces arise due to the planar deformation of the individual triangular elements away from their reference configurations. To facilitate a comparison between the current and reference configurations of the elements, each deformed triangular element is mapped on to a common plane with its initial configuration as illustrated in Fig. 4b. From here, the in-plane displacements, u_x and u_y , can be computed at each vertex of the triangle.

Expressions for the nodal forces, $F_x^{s,i}$ and $F_y^{s,i}$, are obtained via the principle of virtual work for a triangular element, which in terms of the virtual displacements, δu_x^i and δu_y^i , can

be expressed as:

$$\delta W_s = \sum_{i=1}^3 (\delta u_x^i F_x^{s,i} + \delta u_y^i F_y^{s,i}) \quad (16)$$

where, as in Fig. 4b, we use the superscripts $i = 1, 2, 3$ to label quantities defined at the three vertices of the triangle.

The work due to in-plane stretches can be expressed in terms of a constitutive law describing the strain energy per unit area of the element. For simplicity, the areal strain energy density is assumed to be a function of the principle stretch ratios, λ_1 and λ_2 . The stretch ratios are constant on a given element and thus the virtual work for an element is given by $\delta W_s = A_0 \delta W$ where A_0 is the initial area of the element and δW is the first variation of the selected strain energy law.

The first variation of the strain energy function, δW , is computed using the chain rule resulting in the following expression for virtual work of a triangular element due to displacements, δu_x^i and δu_y^i :

$$\delta W_s = A_0 \sum_{k=1}^3 \left[\delta u_x^k \left(\frac{\partial \lambda_1}{\partial u_x^k} \frac{\partial W}{\partial \lambda_1} + \frac{\partial \lambda_2}{\partial u_x^k} \frac{\partial W}{\partial \lambda_2} \right) + \delta u_y^k \left(\frac{\partial \lambda_1}{\partial u_y^k} \frac{\partial W}{\partial \lambda_1} + \frac{\partial \lambda_2}{\partial u_y^k} \frac{\partial W}{\partial \lambda_2} \right) \right]. \quad (17)$$

Equating the right-hand sides of Eqs. (16) and (17) and invoking the arbitrary nature of the virtual displacements gives us the following expression for the nodal forces due to in-plane tensions:

$$\begin{aligned} F_x^{s,i} &= A_0 \frac{\partial W}{\partial \lambda_1} \frac{\partial \lambda_1}{\partial u_x^i} + A_0 \frac{\partial W}{\partial \lambda_2} \frac{\partial \lambda_2}{\partial u_x^i}, \quad i = 1, 2, 3 \\ F_y^{s,i} &= A_0 \frac{\partial W}{\partial \lambda_1} \frac{\partial \lambda_1}{\partial u_y^i} + A_0 \frac{\partial W}{\partial \lambda_2} \frac{\partial \lambda_2}{\partial u_y^i}, \quad i = 1, 2, 3. \end{aligned} \quad (18)$$

The forces $F_x^{s,i}$ and $F_y^{s,i}$ are expressed in terms of the local basis, which are then mapped back to the physical coordinates and added to the node's Lagrangian force term as discussed in Ref.⁴⁷. For example, on a mesh with 5120 triangles, each node is the vertex of 5 or 6 triangles and thus the full elastic force at a given Lagrangian node is the sum of the forces at each of these five or six triangles.

The derivatives in Eq. (18) are computed using a linear finite element method, with linear shape functions, N^i , $i = 1, 2, 3$, where N^1 , is defined as

$$N^1(x, y) = \frac{1}{2A_0} [(y^2 - y^3)k + (x^3 - x^2)y + x^2y^3 - x^3y^2] \quad (19)$$

and N^2 and N^3 can be obtained by cycling the indices from $1 \rightarrow 2 \rightarrow 3 \rightarrow 1$. $2A_0$ is twice the area of the element and is computed as follows:

$$2A_0 = |(y^2 - y^3)x^1 + (x^3 - x^2)y^1 + x^2y^3 - x^3y^2|. \quad (20)$$

In turn, the spatial dependence of the displacement on the element can be expressed as

$$\begin{aligned} u_x(x, y) &= N^1(x, y)u_x^1 + N^2(x, y)u_x^2 + N^3(x, y)u_x^3 \\ u_y(x, y) &= N^1(x, y)u_y^1 + N^2(x, y)u_y^2 + N^3(x, y)u_y^3. \end{aligned} \quad (21)$$

The remaining quantities needed for the computation of the elastic forces are the principle stretch ratios, λ_1 and λ_2 . These are obtained from the eigenvalues of the two-dimensional right Cauchy-Green tensor, \mathbf{G} , whose components are given by:

$$\begin{aligned} G_{11} &= \left(1 + \frac{\partial u_x}{\partial x}\right)^2 + \left(\frac{\partial u_y}{\partial x}\right)^2 \\ G_{22} &= \left(1 + \frac{\partial u_y}{\partial y}\right)^2 + \left(\frac{\partial u_x}{\partial y}\right)^2 \\ G_{21} = G_{12} &= \left(1 + \frac{\partial u_x}{\partial x}\right)\left(\frac{\partial u_y}{\partial y}\right) + \left(1 + \frac{\partial u_y}{\partial y}\right)\left(\frac{\partial u_x}{\partial x}\right). \end{aligned} \quad (22)$$

The derivatives of the in-plane displacements, u and v , in Eq. (22) for $G_{21} = G_{12}$ are computed by differentiating their linear representations given by Eq. (21). Finally, the principle stretch ratios are expressed in terms of the components of \mathbf{G} as follows:

$$\begin{aligned} \lambda_1^2 &= \frac{1}{2} \left[G_{11} + G_{22} + \sqrt{(G_{11} - G_{22})^2 + 4G_{12}^2} \right] \\ \lambda_2^2 &= \frac{1}{2} \left[G_{11} + G_{22} - \sqrt{(G_{11} - G_{22})^2 + 4G_{12}^2} \right]. \end{aligned} \quad (23)$$

2. Bending membrane models

The resistance to bending and the prevention of buckling is relevant in many membrane-bounded bodies, particularly biological ones. The implementation of bending is not trivial and it is computationally intricate. In fact, it has been the subject of several reviews^{55,56}. Since there are many ways to implement bending, for simplicity, we focus on the two most common approaches, one for the continuum approach and another for the discrete approach. We refer the reader to Ref.^{55,56} for bending models and numerical implementations. In line with the continuum approach, one of the most popular bending formulations is that of Helfrich⁵⁷

$$W_B = \frac{E_B}{2} \int_A (2\kappa - c_0)^2 dA + E_G \int_S \kappa_G dA, \quad (24)$$

where κ is the mean curvature and κ_G is the Gaussian curvature, c_0 is the spontaneous curvature (curvature for which the bending energy is minimal). It has been shown that the bending force acting on node i can be written as^{58,59}

$$\mathbf{F}_i^b = E_B [(2\kappa + c_0)(2\kappa^2 - 2\kappa_g - c_0\kappa) + 2\Delta_{LB}\kappa] \mathbf{n} \quad (25)$$

where \mathbf{n} is the outwards normal vector to the surface and Δ_{LB} is the Laplace-Beltrami operator. Calculation of Eq. (25) and $\Delta_{LB}\kappa$ can be found in Ref.^{55,56,60}.

3. Area and volume constraints

In order to impose area and volume conservation it may be necessary to include appropriate constraints. This will depend

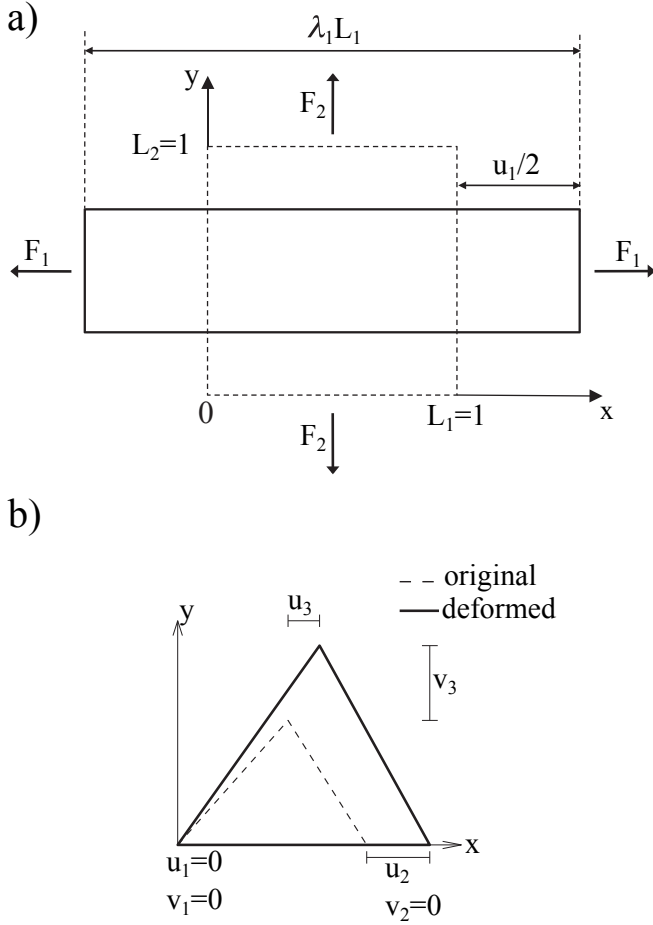


FIG. 4. a) Example of a deformation of a 2D sheet due to forces F_1 and F_2 . Deformation in the x_1 direction is characterised by the stretch ratio λ_1 or by the displacement u_1 (same in the x_2 direction). λ_1 and λ_2 are the stretch ratios in two principle directions, defined as the ratio of the final to the initial length. b) Computation of the deformation is done by mapping both the original and the deformed triangles to a common plane.

on the problem at hand. In some cases like a capsule in shear flow, the volume change is negligible and it is not necessary to impose volume conservation. The area and volume energy constraints can be enforced by adding the energy terms⁴⁹

$$\begin{aligned} W_A &= \frac{k_a}{2} \frac{(A - A_0)^2}{A_0}, \\ W_V &= \frac{k_v}{2} \frac{(V - V_0)^2}{V_0}. \end{aligned} \quad (26)$$

where k_a and k_v are the area and volume coefficients that control the strength of the force which regulates the change in total area A and the volume V from the initial area A_0 and volume V_0 . While A_0 and V_0 are input parameters, A and V need to be computed at every time step. From Eqs. (26) we find

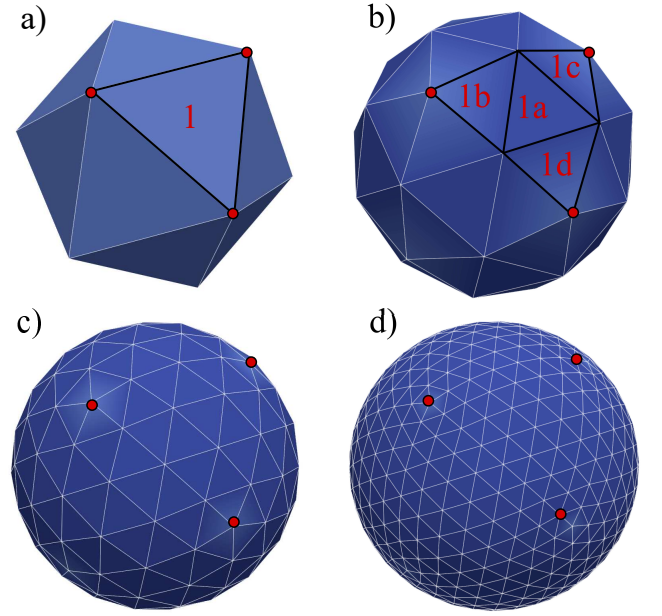


FIG. 5. Loop subdivision mesh. The mesh is started from a solid such as an icosahedron (or other initial shapes such as a pyramid) which has 20 sides and 12 nodes. A triangular surface element is divided into 4. There are 3 levels of refinement shown: a) to b), b) to c) and c) to d). For clarification, we highlight an initial triangle 1 which is divided into triangles 1a, 1b, 1c, and 1d. The red points just indicate the nodes of the initial face element.

that the corresponding forces are

$$\begin{aligned} \mathbf{F}_i^A &= k_a \frac{(A - A_0)}{A_0} \frac{\partial A}{\partial \mathbf{x}_i}, \\ \mathbf{F}_i^V &= k_v \frac{(V - V_0)}{V_0} \frac{\partial V}{\partial \mathbf{x}_i}. \end{aligned} \quad (27)$$

More details and computation of $\frac{\partial A}{\partial \mathbf{x}_i}$ and $\frac{\partial V}{\partial \mathbf{x}_i}$ may be found in Ref.⁴⁹. While A can be calculated by summing the elemental areas (e.g. triangles), the calculation of volume requires a more sophisticated approach. An efficient way to calculate V is described in Ref.⁶¹. We can also express Eqs. (26) as⁶²,

$$\begin{aligned} \mathbf{F}_i^A &= -2k_s \frac{A - A_0}{A_0} \kappa \mathbf{n}, \\ \mathbf{F}_i^V &= -k_v \frac{V - V_0}{V_0} \mathbf{n}, \end{aligned} \quad (28)$$

where \mathbf{n} is the outwards normal to the surface and κ is the mean curvature. These constraints for area and volume are also used in models which employ a discrete approach.

Finally, since a node can be the vertex of multiple surface elements, the total force $\mathbf{F}_i = \mathbf{F}_i^s + \mathbf{F}_i^b + \mathbf{F}_i^A + \mathbf{F}_i^V$ acting on node i is,

$$\mathbf{F}_i = \sum_j (\mathbf{F}_i)_j, \quad (29)$$

where j runs over each surrounding element.

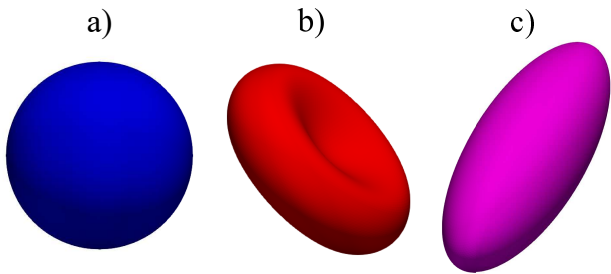


FIG. 6. Examples of different shapes that can be used in the lattice-Boltzmann method with finite elements and immerse boundary. (a) is a sphere, (b) is a biconcave shell and (c) is an ellipsoid. An icosahedron was used and there were 5 subdivisions so the total number of elements is $N_e^5 = 20 \times 4^5 = 20480$ faces.

B. Discrete approach

An alternative approach models the membrane elasticity from molecular information, as first proposed in Ref.⁶³, and subsequently widely used^{64,65}. The idea originated from molecular dynamics which models the interactions between particles. Theoretically, it is possible to model the fluid-structure interaction flows using molecular dynamics. However, the computational cost of molecular dynamics is prohibitively expensive to reach the length and time scales relevant to the motion and deformation of flexible objects. Addressing this regime requires a mesoscale method. Using a discrete network of springs and particles is one of the approaches as many atoms are conceptualised as one molecular cluster (or virtual particle), then, an effective interaction potential between each particle may be defined to model the mechanical response of the system. The number of degrees of freedom is reduced, and the time and length scales are increased. Each particle position is updated following Newton's law, where the force field is derived from the potential energy between the particles. Other forces such as fluid forces and particle-particle repulsion are also taken into account. During the discretization process, the details of individual atomic dynamics are lost, but the longer-range temporal and spatial phenomena are preserved.

For a discrete membrane model, a number of potentials have been used, from the simple linear harmonic potential to a complex worm-like-chain (WLC) potential and the finite extensible nonlinear elastic (FENE) potential. One of the advantages of this approach for membrane modelling is the simplicity of mathematical description and programming. This approach has been shown to provide consistent predictions with energy density functions used in the continuum model^{43,63}. The total energy of a membrane is

$$U = U_{\text{stretch}} + U_{\text{bending}} + U_{\text{area}} + U_{\text{volume}}, \quad (30)$$

where U_{volume} is included only for 3D simulations. We use the notation U (instead of W) in order to differentiate from the continuum approach. Once again, the nodal force at node i at

position x_i derived from the potential energy is given by

$$\mathbf{F}_i = -\frac{\partial U(x_i)}{\partial x_i}. \quad (31)$$

Full derivations are not shown but can be found in Ref.⁶⁶.

1. Elastic membrane models

A harmonic stretching potential can be used to model the stretching energy as

$$U_{\text{stretch}} = U_{\text{HAR}} = \frac{1}{2} k_s \sum_{j=1, \dots, N_s} (l_j - l_{j0})^2, \quad (32)$$

where k_s is the stretching constant, l_j is the length of the j -th spring, and l_{j0} is the corresponding equilibrium spring length. The total stretching energy should be summed over all the line segments. This model has been used to model malaria-infected RBCs⁶⁷ and mesoscopic blood flow⁶⁸. However, this simple linear model cannot capture the nonlinear behaviour of many membranes, such as a cell membrane. An exponential relationship for mechanical stiffness k_s related to the bond stretch ratio (ι) is included to capture the nonlinear behaviour⁶⁹. The exponential form of the spring constant can be expressed as $k_s = k_{s0} e^{2(\iota-1)}$, where ι is defined as $\iota = l/l_0$ with l the spring's length and l_0 is the spring's equilibrium/initial length. Similarly, other nonlinear potentials may be used to model the membrane stretching energy. The two most popular nonlinear potentials⁶⁴ are the worm-like chain (WLC) potential and the finite extensible nonlinear elastic (FENE) potential. Explicitly, they are defined as

$$U_{\text{WLC}} = \frac{k_B T l_m}{4p} \frac{3x^2 - 2x^3}{1-x}, \quad U_{\text{FENE}} = -\frac{k_s}{2} l_m^2 \log[1-x^2], \quad (33)$$

where $x = l/l_m \in (0, 1)$, l_m is the maximum spring extension, p is the persistence length, k_B is the Boltzmann constant, T is the temperature, k_s is the FENE spring constant. These two models are very similar in terms of force strain relations.

Note that these springs (FENE and WLC) only provide attractive forces, thus they tend to reduce the area. A repulsive force field should be combined with these nonlinear potentials. Ref.⁶⁴ proposed two potentials, one of which is an inverse power repulsive potential (U_{POW}) that is based on the spring length. This means

$$U_{\text{stretch}} = U_{\text{WLC}} + U_{\text{POW}} \quad \text{or} \quad U_{\text{stretch}} = U_{\text{FENE}} + U_{\text{POW}}, \quad (34)$$

where the inverse power repulsive potential is given by

$$U_{\text{POW}} = \frac{k_p}{(n-1)l^{n-1}} \quad n > 0, n \neq 1 \quad (35)$$

and k_p is the repulsive stiffness. Finally, the forces for Eqs.

(33) and (35) are

$$\begin{aligned} \mathbf{F}_{\text{WLC}}(l) &= -\frac{k_B T}{p} \left(\frac{1}{4(1-x)^2} - \frac{1}{4} + x \right) \hat{l}_{ij}, \\ \mathbf{F}_{\text{FENE}}(l) &= -\frac{k_s l}{1-x^2} \hat{l}_{ij}, \\ \mathbf{F}_{\text{POW}}(l) &= \frac{k_p}{l^m} \hat{l}_{ij}, \end{aligned} \quad (36)$$

where $x = l/l_m$ and $\hat{l}_{ij} = \vec{l}_{ij}/l$ is the vector of unit length between nodes i and j .

2. Bending membrane models

A popular and simplified expression for the bending energy often used with the discrete approach is,

$$U_{\text{bending}} = k_b \sum_{j \in 1 \dots N_b} [1 - \cos(\theta_k - \theta_{k0})], \quad (37)$$

where k_b is the bending constant, θ_k is the instantaneous angle formed by the two outward surface normals of two adjacent triangular meshes that share the edge k . θ_{k0} is the corresponding equilibrium or spontaneous angle. The corresponding force Eq. (37) is given by

$$\mathbf{F}_i^b = -k_b \sin(\theta_k - \theta_{k0}) \frac{\partial \theta_k}{\partial \mathbf{x}_i}. \quad (38)$$

Details on the calculation of $\frac{\partial \theta_k}{\partial \mathbf{x}_i}$ can be found in Ref.⁴⁹.

3. Area and volume constraints membrane models

Area and volume constraints U_A and U_V are similar to those already used in the continuum approach i.e. Eqs (26), (27) and (28).

C. Linking fluid to structure

Fluid-structure interaction (FSI) problems are generally driven by the interaction of two different components: one fluid and one solid. Generalisations for multiple fluids and solids are possible. Fluid-structure interaction problems are important in many scientific and engineering applications, such as paint pigments, polymers, gels, proteins and red blood cells flow in the heart⁷⁰. However, they are also challenging due to their nonlinear and multiscale nature. Generally, an analytical solution to the coupled system of equations is impossible. Thus, numerical methods have been developed to solve the fluid and structure dynamics simultaneously. The interface boundary conditions are crucial to the coupled FSI problems. Currently, there are two general approaches. The first is the Arbitrary Lagrangian-Eulerian (ALE) method⁷⁰. In this approach, the mesh used for the fluid is neither fixed in space as in the Eulerian description nor moved with the fluid

as in the Lagrangian description. Instead, the mesh of the fluid can move in any other prescribed way. On the interface between fluid and solid, the velocity and stress should be continuum. The mesh of fluid conforms to the mesh of the solid. Thus, it is straightforward to impose boundary conditions on the fluid-solid interface, in an accurate and efficient way. However, as solids are subjected to large translations and rotations, re-meshing is usually used to avoid mesh distortion or entanglement. This mesh regeneration is cumbersome during the computation. As opposed to the accurately captured fluid-solid boundaries in the ALE method, the immersed boundary method (IBM) was introduced by Peskin⁴⁶ using a non-boundary fitting method. Specifically, two independent meshes are used for the fluid and solid. The existence of solids is represented by the solid boundary force spread out into the fluid. The IBM approach eliminates the re-meshing procedure in the ALE, which is very efficient in FSI modelling.

The mechanics of the solid and fluid flow need to be solved. This can be done in two ways: a partitioned way where the structural mechanics and flow equations are solved separately or a monolithic way where they are solved simultaneously. FSI problems using the LBM often use the IBM as a coupling algorithm. This allows software modularity and different, possibly more efficient algorithms can be used to solve the structural mechanics.

This section will discuss the technical details of IBM and its coupling with the LBM. Other coupling techniques such as the stress integration approach⁷¹ and friction coupling approach^{21,72-74} are briefly mentioned. The IBM was selected due to its efficiency and popularity. It was first proposed by Peskin to study blood flow in the heart⁴⁶ using vortex methods. The fluid is solved on a spatially fixed Eulerian grid, while the immersed solids are modelled using a moving Lagrangian mesh, which is not constrained to the geometric layout of the Eulerian fluid grid. Data is exchanged between the two domains through nodal interpolation. The coupling scheme enforces velocity continuity at the fluid-structure boundary and transfers forces from the structure back into the fluid through an effective force density. This two-way coupling automatically handles immersed body contact and prevents solid penetration through the development of restoring forces in the fluid. The approach has been used for a variety of fluid-structure interaction problems, including the simulation of jellyfish⁷⁵, blood flow^{10,76,77} and platelet migration⁷⁸. Comprehensive reviews of IBM and its applications can be found in^{46,79}. The immersed structure can be viewed as a parametric surface $X(p, q, r, t)$, where p, q, r are curvilinear coordinates for the structure in a Lagrangian description and t is the time. The fluid domain is described by Eulerian coordinates \mathbf{x} . The force $\mathbf{g}(\mathbf{x}, t)$ exerted by the structure on the fluid is interpolated as a source term in the momentum equation using

$$\mathbf{g}(\mathbf{x}, t) = \int \mathbf{F}(p, q, r, t) \delta(\mathbf{x} - X(p, q, r, t)) dp dq dr, \quad (39)$$

where $\mathbf{F}(p, q, r, t)$ is the force density for the structure. Typically, it is derived from energy density functions. $\delta(\mathbf{x})$ is the three-dimensional delta functions $\delta(x_1) \delta(x_2) \delta(x_3)$ where x_1, x_2, x_3 are the Cartesian components of the position vector

\mathbf{x} . Similarly, the moving structure velocity is updated based on the local fluid velocity through interpolation using

$$\mathbf{u}(\mathbf{X}(p, q, r, t), t) = \int \mathbf{u}(\mathbf{x}, t) \delta(\mathbf{x} - \mathbf{X}(p, q, r, t)) d\mathbf{x}, \quad (40)$$

where $\mathbf{u}(\mathbf{X}(p, q, r, t), t)$ is the structural velocity, $\mathbf{u}(\mathbf{x}, t)$ is the fluid velocity of the fluid domain \mathbf{x} at time t . $\delta(\mathbf{x})$ is the same function as used in Eqs (39) and (40) is the continuity for the velocity on the fluid-structure interface.

The concept of IBM coupling is also illustrated in Fig. 7 where the empty dots represent fluid nodes, while full red dots represent the solid structure. The solid velocity is interpolated from the local fluid velocity. The contribution of each neighbour fluid node and how many nodes should be selected is determined by $\delta(\mathbf{x})$. For example, Fig. 7 (left) shows that the velocity of the structural central node is interpolated from four nearby nodes within the shaded square frame. Similarly, the structural force will be spread to the four neighbouring fluid nodes.

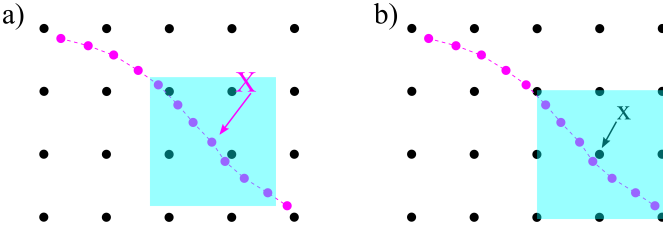


FIG. 7. The two-way coupling between the fluid and the structure in the immersed boundary method. a) The structural velocity $\mathbf{u}(\mathbf{X}, t)$ is interpolated from neighbouring fluid nodes within the shaded square box. The contribution from a fluid node is weighted by the $\delta(\mathbf{x})$ function. b) The structural force will be spread out into local fluid nodes as a force density. We see that the fluid node \mathbf{x} will receive a force contribution from the magenta nodes within the shaded box. The distribution of the force among fluid nodes is determined by the $\delta(\mathbf{x})$ function as well. The number of neighbouring nodes to spread the force can vary.

1. Spatial and temporal discretization

Once the coupling scheme has been established, the spatial and temporal discretization of the IBM equations, (39) and (40), is needed for the numerical implementation of the IBM. Following Ref.⁴⁶, we discuss the spatial discretization first, the choice of $\delta(\mathbf{x})$ next, and the temporal integration scheme last. The spatial discretization of the Eulerian grid, denoted by g_x is a set of points with equal spacing in Cartesian coordinates, e.g., $\mathbf{x} = (x_j, y_j, z_j) \Delta x$, where Δx is the spacing, (x_j, y_j, z_j) are the components of the position in each direction. This spatial discretization is also consistent with the lattice Boltzmann fluid solver, which means $\Delta x = \delta x$ and $\Delta t = \delta t$. Similarly, the spatial discretization of the Lagrangian grid, denoted by G_s , is the set of (p, q, r) of the form $(p_k \delta p, q_k \delta q, r_k \delta r)$, where (p_k, q_k, r_k) are integers. Ref⁴⁶ also suggested that $\delta s < \frac{\Delta x}{2}$, $s \in \{p, q, r\}$ should be required

to avoid fluid leaking. Ref⁴⁹ shows that the mesh ratio between solid and fluid for small deformations, e.g., $\frac{\delta s}{\Delta x}$, can be safely chosen within the range (0.5, 1.5) without significantly influencing the physical results. However, the membrane resolution must be sufficiently high to handle regions with large local curvature. The force spreading equation (39) becomes

$$\mathbf{g}(\mathbf{x}, t) = \sum_{(p, q, r) \in G_s} \mathbf{F}(p, q, r, t) \delta_\Delta(\mathbf{x} - \mathbf{X}(p, q, r, t)) \Delta p \Delta q \Delta r. \quad (41)$$

Notice that $\mathbf{F}(p, q, r, t)$ is the force density among solid structures. Let us define $\mathcal{F} = \mathbf{F}(p, q, r, t) \Delta p \Delta q \Delta r$. \mathcal{F} can be viewed as the integration of the force density \mathbf{F} over the element of volume $dv = \Delta p \Delta q \Delta r$, which is the force term applied to each node. The Lagrangian nodes of the solid can be indexed as i without losing any generality. Equation (41) can be reduced to

$$\mathbf{g}(\mathbf{x}, t) = \sum_{i \in G_s} \mathcal{F}_i \delta_\Delta(\mathbf{x} - \mathbf{X}_i). \quad (42)$$

The velocity interpolation formula can be discretized as

$$\mathbf{u}(\mathbf{X}_i, t) = \sum_{x \in g_x} \mathbf{u}(\mathbf{x}, t) \delta_\Delta(\mathbf{x} - \mathbf{X}_i) \Delta x^3. \quad (43)$$

In the lattice Boltzmann method, the spatial step and the time step in LB units are usually assumed unity, e.g., $\Delta x = 1, \Delta t = 1$. Thus, Eq. (43) can be reduced to

$$\mathbf{u}(\mathbf{X}_i, t) = \sum_{x \in g_x} \mathbf{u}(\mathbf{x}, t) \delta_\Delta(\mathbf{x} - \mathbf{X}_i). \quad (44)$$

Reference⁴⁶ showed that the discretized $\delta_\Delta(\mathbf{x})$ function has to meet some restrictions and properties to make sure that mass, force, and torque are the same if they are evaluated from Eulerian or Lagrangian variables. One of the assumptions made here is that $\delta_\Delta(\mathbf{x})$ is given by the triple product of a scalar function $\phi(x)$

$$\delta_\Delta(\mathbf{x}) = \phi(x) \phi(y) \phi(z), \quad (45)$$

where (x, y, z) are the three components of the position vector \mathbf{x} . Here we do not focus on the details of the $\phi(x)$ function. Instead, we just want to point out the most widely used four-point interpolation function which is,

$$\phi(x) = \begin{cases} 0, & |x| \geq 2 \\ \frac{1}{8} \left(5 - 2|x| - \sqrt{-7 + 12|x| - 4x^2} \right), & 1 \leq |x| \leq 2 \\ \frac{1}{8} \left(3 - 2|x| + \sqrt{1 + 4|x| - 4x^2} \right), & 0 \leq |x| < 1. \end{cases} \quad (46)$$

Reference⁴⁶ noted that $\phi(x)$ is also well approximated by a simple formula

$$\phi(x) = \begin{cases} 0, & \text{otherwise} \\ \frac{1}{4} \left(1 + \cos\left(\frac{\pi x}{2}\right) \right), & |x| \leq 2. \end{cases} \quad (47)$$

However, Eq. (46) is much faster as it involves evaluating polynomial functions rather than the $\cos(x)$ function. Since

the fluid and solid are solved alternatively, this IBM coupling is a partitioned approach. To obtain a second-order accurate scheme in temporal discretization, Peskin came up with a time integration scheme based on the midpoint rule⁴⁶. For easiness of the discussion, the solution at time step n will be denoted by a superscript on the variable. So let us assume we have the structural position X_i^n at time step n , the intermediate position at time step $n + \frac{1}{2}$ is calculated using

$$\mathbf{X}_i^{n+\frac{1}{2}} = \mathbf{X}_i^n + \frac{\Delta t}{2} \sum_{\mathbf{x} \in G_x} \mathbf{u}^n \delta_{\Delta}(\mathbf{x} - \mathbf{X}_i) \Delta x^3. \quad (48)$$

With the newly obtained solid position at the $n + \frac{1}{2}$ time step, the structural force can be evaluated as

$$\mathcal{F}_i^{n+\frac{1}{2}} = \mathbf{F}_i^{n+\frac{1}{2}} \Delta p \Delta q \Delta r = \text{StructureSolver} \left(\mathbf{X}_i^{n+\frac{1}{2}} \right), \quad (49)$$

where StructureSolver is the procedure used to calculate all the structure forces applied to each structural node (e.g. nodes on a circular capsule). Next, the structure force $\mathcal{F}_i^{n+\frac{1}{2}}$ will be spread out into the fluid through

$$\mathbf{g}^{n+\frac{1}{2}}(\mathbf{x}) = \sum_{\mathbf{X} \in G_s} \mathcal{F}_i^{n+\frac{1}{2}} \delta_{\Delta}(\mathbf{x} - \mathbf{X}_i) A_b. \quad (50)$$

With the force density, the fluid solver will update the fluid velocity \mathbf{u}^{n+1} through

$$\mathbf{u}^{n+1} = \text{FluidSolver} \left(\mathbf{g}^{n+\frac{1}{2}} \right). \quad (51)$$

The FluidSolver could be any method in CFD. The LBM is used in this review. Finally, the solid position at time $n + 1$ is updated as

$$\mathbf{X}_i^{n+1} = \mathbf{X}_i^n + \Delta t \sum_{\mathbf{x} \in G_x} \mathbf{u}^{n+1} \delta_{\Delta}(\mathbf{x} - \mathbf{X}_i) \Delta x^3. \quad (52)$$

2. Lubrication corrections

When the gap between particles or between particles and the wall is equal to or less than the resolution of the discretization, the fluid flow can no longer be resolved in this region. In most cases this happens when the gap is less than one lattice spacing. To solve this, there are two alternative solutions. The first one is to use a finer mesh for the whole fluid system (or just near the region in question if possible). This would lead to a more expensive simulation. Depending on the problem a slightly finer mesh might prove to be enough. The second approach is to introduce a lubrication force that mimics the repulsive force of the fluid being squeezed out of the gap. This second approach is computationally more manageable. This idea has been incorporated into the LBM^{80–82}, using lubrication theory. The lubrication force between two rigid spheres is

$$\mathbf{F}_{ij}^{\text{lub}} = -\frac{3\pi\mu r}{s} \hat{\mathbf{x}}_{ij} \hat{\mathbf{x}}_{ij} \cdot (\mathbf{u}_i - \mathbf{u}_j), \quad (53)$$

where r is the spherical radius, μ is the fluid dynamic viscosity, s is the dimensionless gap $s = R/r - 2$ where R is the central distance between two spheres. \mathbf{x}_{ij} is the position vector difference between sphere i and j , defined as $\mathbf{x}_{ij} = \mathbf{x}_i - \mathbf{x}_j$, $\hat{\mathbf{x}}_{ij}$ is the unit vector. \mathbf{u} is the sphere's velocity. Equation (53) can also be extended to the case where a sphere approaches a stationary wall or object by setting $\mathbf{u}_j = 0$.

For deformable bodies, a repulsive force between any two nodes of two meshes in close proximity is sufficient⁸³. This force is zero for node-to-node distances larger than one lattice constant and increases as $1/r^2$ at smaller distances

$$\mathbf{g}_{ij}^{\text{int}} = \begin{cases} -\kappa_{\text{int}} \left(d_{ij}^{-2} - 1 \right) \frac{d_{ij}}{d_{ij}} & \text{for } d_{ij} < 1, \\ 0 & \text{for } d_{ij} \geq 1 \end{cases}$$

where d_{ij} is the distance between the two nodes i and j , κ_{int} is a constant regulating the strength and $\mathbf{g}_{ji}^{\text{int}} = -\mathbf{g}_{ij}^{\text{int}}$.

3. Other coupling schemes

Here we discuss only the no-slip boundary conditions between fluid and structure, which consists of imposing velocity and force continuity along the interface

$$\begin{aligned} u_f &= u_s & \text{on } \Upsilon \\ \sigma_{ij}^f n_j &= \sigma_{ij}^s n_j & \text{on } \Upsilon \end{aligned} \quad (54)$$

where u_f and u_s are the fluid and solid velocity, Υ is the interface between the solid and the fluid. σ_{ij} is the stress tensor with superscript f and s representing the fluid and solid, respectively. n_j is the surface normal. In the IBM, the solid velocity is interpolated from the fluid, as shown in Eq. (40), while the force is spread into the fluid, as indicated by Eq. (39). The reverse approach can also be used^{71,84}, where we apply first the fluid stress to the structure, then solve the structural response, and finally impose the structural velocity as a boundary condition on the fluid. This method is called the stress integration approach^{71,85}. The total force acting on the structure is

$$T_i = \int \sigma_{ij} n_j dA \quad (55)$$

where dA is the differential area over the interface. The stress tensor σ_{ij} is given by

$$\sigma_{ij} = -p \delta_{ij} + \rho v (u_{i,j} + u_{j,i}). \quad (56)$$

The pressure term p can be evaluated using $p = \rho c_s^2$. Following Ref.⁸⁶, the deviatoric shear stress in the LBM $\tau_{ij} := \rho v (u_{i,j} + u_{j,i})$ can be evaluated as

$$\tau_{ij} = -\left(1 - \frac{\omega}{2}\right) \sum_{\alpha} \left(\xi_{\alpha i} \xi_{\alpha j} - \frac{\delta_{ij}}{D} \xi_{\alpha} \cdot \xi_{\alpha} \right) f_{\alpha}^{\text{neq}} \Delta t \quad (57)$$

where $\omega = \frac{\Delta t}{\tau}$, τ is the relaxation parameter for the LBM. α is the index of the discretized velocity vector, f_{α}^{neq} is the

non-equilibrium part of the density distribution defined as $f_\alpha^{neq} = f_\alpha - f_\alpha^0$ with f_α^0 calculated from Eq. (6). ξ_α is the discretized velocity vector. With the stress calculated from the LBM using Eqs. (56) and (57), the force applied to the structure can be evaluated by a dot product between the surface normal and the stress tensor using the second equation in (54).

For soft matter systems, the flows are often isothermal, incompressible, and at low Reynolds numbers. Thus, it is natural to use the Stokes friction force to couple the immersed solids and fluids^{72–74,87}. In Ref.⁷³, polymer monomers are treated as points with a friction force

$$F = -\zeta (u_s - u_f), \quad (58)$$

where ζ is the friction coefficient, which may be different from that given by Einstein's relation for diffusion. u_s, u_f are solid point and local fluid velocities, respectively. The local fluid velocity u_f could be interpolated from nearby fluid nodes. The friction force F will be applied to the solid, together with other forces to determine the motion of the particles. A force with the same magnitude but with a reversed direction $-F$ is applied to the local fluid nodes. For example, the force density $-F/\delta x^3$ will be spread to 8 local fluid nodes, as shown in Ref.^{72,73}. Tuning might be necessary for an appropriate choice of the friction coefficient to reduce the effect of slip.

IV. FLUID-FLUID BASED METHODS

This section comprises an overview of some of the most popular multicomponent models for droplets and emulsions using the lattice Boltzmann method. The mesoscopic nature of LBM allows the easy incorporation of inter-particle forces. The interface between components or phases results from the included inter-particle forces, however, they are often under-resolved and considered to be diffusive in order to allow for reasonable computation times. From each individual model's inception, there have been numerous modifications and improvements enabling a wider range of parameters to be explored and reducing undesirable artefacts. From the numerous works investigating multiphase/ multicomponent phenomena with different models, it is clear that no model offers the best performance in all respects. First, we present the multicomponent formulation of each method and then we explain how frustrated coalescence can be achieved.

A. Colour Modelling

One of the first multicomponent models was developed in Ref.⁸⁸. This model extended the single-phase lattice-gas cellular automaton (LGCA) to allow for two immiscible components with surface tension. The standard indistinguishable particles of the LGCA are replaced by two (or more) distinct particles, usually referred to as red and blue particles. The rules of the model are similar to the standard LGCA, in that the collisions conserve the number of red and blue particles. However, additional rules include encouraging the grouping of like

colours and the generation of surface tension. The model was subsequently incorporated into the LBM in Ref.⁸⁹ and later, in Ref.⁹⁰ the model was modified to allow for variation in density and viscosity ratios. Another key development was proposed in Ref.⁹¹, namely, to add a recolouring step which significantly reduces the computational requirements while minimising the spurious currents and removing the lattice pinning effect. The model works by introducing the distribution function for each of the fluid components $f_{\alpha,k}(\mathbf{x}, t)$, where k is the component index. The evolution equation is thus expressed as

$$f_{\alpha,k}(\mathbf{x} + \xi_\alpha \Delta t, t + \Delta t) = f_{\alpha,k}(\mathbf{x}, t) + \Omega_{\alpha,k}(\mathbf{x}, t), \quad (59)$$

where $\Omega_{\alpha,k}$ is the multistage collision operator expressed as

$$\Omega_{\alpha,k} = \left[\Omega_{\alpha,k}^{(1)} + \Omega_{\alpha,k}^{(2)} \right] \Omega_{\alpha,k}^{(3)}. \quad (60)$$

Each of these collision operators serves a specific purpose:

- $\Omega_{\alpha,k}^{(1)}$ is the normal single-phase collision operator for each component;
- $\Omega_{\alpha,k}^{(2)}$ is the perturbation operator, generating the interfacial tension;
- $\Omega_{\alpha,k}^{(3)}$ is the recolouring operator responsible for phase separation.

Macroscopic quantities are recovered by taking the usual moments of $f_{\alpha,k}(x, t)$:

$$\begin{aligned} \rho_k &= \sum_{\alpha} f_{\alpha,k}, \\ \rho \mathbf{u} &= \sum_{\alpha,k} \xi_{\alpha} f_{\alpha,k}, \end{aligned} \quad (61)$$

where $\rho = \sum_k \rho_k$. Therefore, the velocity \mathbf{u} is referred to as the colour-blind velocity. The perturbation step, which generates the surface tension at the interface between two components is given by

$$\Omega_{\alpha,k}^{(2)} = \frac{A_k}{2} |\nabla \rho| \left[w_{\alpha} \frac{(\xi_{\alpha} \cdot \nabla \rho)^2}{|\nabla \rho|^2} - B_{\alpha} \right], \quad (62)$$

where $\nabla \rho$ is the colour gradient, A_k is responsible for controlling the strength of the surface tension and B_{α} are constants specific to the chosen velocity set. For the D2Q9 velocity set, B_{α} are given by

$$\begin{aligned} B_0 &= -\frac{\chi}{3\chi + 6} c^2, \quad B_{1,\dots,4} = \frac{\chi}{6\chi + 12} c^2 \quad \text{and} \\ B_{5,\dots,8} &= \frac{1}{6\chi + 12} c^2. \end{aligned} \quad (63)$$

Likewise, for the D3Q19 velocity set, B_{α} are given by

$$\begin{aligned} B_0 &= -\frac{2 + 2\chi}{3\chi + 12} c^2, \quad B_{1,\dots,6} = \frac{\chi}{6\chi + 24} c^2 \quad \text{and} \\ B_{7,\dots,18} &= \frac{1}{6\chi + 24} c^2, \end{aligned} \quad (64)$$

where χ is a free parameter: Values for B_α and χ are derived in Ref.⁹². Calculation of partial derivatives is necessary for $\nabla\rho$ and it has been shown⁹³ that the following isotropic central difference contributes to enhancing numerical stability and lowering the discretization error,

$$\partial_j \rho(\mathbf{x}, t) \approx \frac{1}{c_s^2 \Delta t} \sum_\alpha w_\alpha \rho(\mathbf{x} + \boldsymbol{\xi}_\alpha \Delta t, t) \xi_{\alpha j}, \quad (65)$$

where j runs through the spatial coordinates. The final step of the colour model is recolouring. The original model of Rothman⁸⁸ involves the minimisation of the work, W , which is given by

$$W(f^r, f^b) = -\nabla\rho \cdot \mathbf{q}(f^r, f^b), \quad (66)$$

where \mathbf{q} is the local or colour flux

$$\mathbf{q}(f^r, f^b) = \sum_\alpha \boldsymbol{\xi}_\alpha (f_\alpha^r - f_\alpha^b). \quad (67)$$

However, this method of recolouring could cause pinning, examples of which include the advection of droplets in a stream becoming pinned to a lattice node below a critical diameter. This was rectified in Ref.⁹¹ by allowing the red and blue components to mix by ensuring symmetric colour distribution with respect to the colour gradient. The post-recolouring particle distributions are expressed as:

$$\begin{aligned} \Omega_\alpha^{r(3)}(f_\alpha^r) &= \frac{\rho_r}{\rho} f_\alpha^r + \mathcal{B} \frac{\rho_r \rho_b}{\rho^2} f_\alpha^{eq}(\rho, \mathbf{u} = 0) \cos(\theta_\alpha), \\ \Omega_\alpha^{b(3)}(f_\alpha^b) &= \frac{\rho_b}{\rho} f_\alpha^b - \mathcal{B} \frac{\rho_r \rho_b}{\rho^2} f_\alpha^{eq}(\rho, \mathbf{u} = 0) \cos(\theta_\alpha), \end{aligned} \quad (68)$$

where \mathcal{B} should be between 0 and 1 and is used for controlling the thickness of the interface, $f_\alpha^r = \sum_k f'_{\alpha,k}$ where $f'_{\alpha,k}$ is the post-collision state after $\Omega_{\alpha,k}^{(1)}$ and $\Omega_{\alpha,k}^{(2)}$ have been applied. The term $\cos(\theta_\alpha)$ is conveniently expressed as

$$\cos(\theta_\alpha) = \frac{\boldsymbol{\xi}_\alpha \cdot \nabla\rho}{|\boldsymbol{\xi}_\alpha| |\nabla\rho|}. \quad (69)$$

The total zero-velocity equilibrium distribution function $f_\alpha^{eq}(\rho, \mathbf{u} = 0) = \sum_k f_{\alpha,k}(\rho, \mathbf{u} = 0)^{eq}$ is given by

$$f_\alpha^{eq} = \rho \left(\phi_\alpha + w_\alpha \left[3\boldsymbol{\xi}_\alpha \cdot \mathbf{u} + \frac{9}{2} (\boldsymbol{\xi}_\alpha \cdot \mathbf{u})^2 - \frac{3}{2} (\mathbf{u})^2 \right] \right) \quad (70)$$

where the weights ϕ_α (along with w_α) are lattice dependent^{94,95}. Further modification of the recolouring step in Eq. (68) to improve spurious velocities, lattice pinning and convergence was done first in Ref.⁹⁴. Additionally, θ_α is the angle between the colour gradient $\nabla\rho$ and the discrete lattice vector $\boldsymbol{\xi}_\alpha$. After the application of all three collision operators, the usual streaming step is applied for each colour.

The benefits of the colour model are that it is straightforward to extend beyond two components, additionally, it allows for independent control over the interface thickness and the surface tension. Recent advancements have also enabled to simulate fluids with moderate density and viscosity ratios. A potential drawback, depending on the modelling requirements is that there is no direct link to thermodynamics. An additional drawback is the generation of spurious velocities at curved interfaces which also occurs in most of the other models.

Frustrated coalescence

In colour modelling, a repulsive force has been used to prevent the coalescence of immiscible droplets⁹⁶⁻⁹⁸. This repulsive force term (operating exclusively on the fluids interfaces) can be introduced to account for any near-contact forces acting between droplets that are closer than the lattice spacing

$$\mathbf{F}_{\text{rep}} = -A_h[h(\mathbf{x})] \mathbf{n} \delta_l, \quad (71)$$

where $A_h[h(\mathbf{x})]$ is the parameter controlling the strength of this repulsive force, \mathbf{n} is a unit normal to the interface and $\delta_l = \frac{1}{2} |\nabla\phi|$ is a function proportional to the phase field $\phi = \frac{\rho^1 - \rho^2}{\rho^1 + \rho^2}$ which confines the repulsive force to the interface. A graphical representation of this force is shown in Fig. 8. $A_h[h(\mathbf{x})]$ can be set equal to a constant A if $h \leq h_{\min}$, it decays as f^{-3} if $h_{\min} < h \leq h_{\max}$ and it is equal to zero if $h > h_{\max}$. For example in Ref.⁹⁸, $h_{\min} = 2$ and $h_{\max} = 4$ lattice spacings. Despite the possibility of other functional forms, this one is generally adequate to prevent droplet coalescence and, more significantly, to accurately describe the physics at various length scales. The repulsive force leads to

$$\begin{aligned} \frac{\partial(\rho\mathbf{u})}{\partial t} + \nabla \cdot (\rho\mathbf{u}\mathbf{u}) &= -\nabla p + \nabla \cdot [\rho\nu(\nabla\mathbf{u} + \nabla\mathbf{u}^T)] \\ &+ \nabla \cdot (\boldsymbol{\Sigma} + \boldsymbol{\pi}l), \end{aligned} \quad (72)$$

which is the NS momentum equation for a multicomponent system, with a surface-localized repulsive term, expressed through the potential function $\nabla\pi$. Including extra forces to frustrate coalescence can in principle be used for any multicomponent method, as will be discussed in the following sections.

B. Free-Energy Modelling

We present a simple free-energy lattice Boltzmann method for binary liquid mixtures^{99,100}. In this method, discrete density distributions $f_{k,\alpha}$ for each k -component model the hydrodynamics and the evolution of a phase field, respectively. This method is a Cahn-Hilliard phase field method for a scalar that specifies the composition of the fluid. Both the fluid flow and evolution of the scalar phase field are solved with the LBM. This scalar advects with the flow and also diffuses towards minimization of a free-energy functional. The functional has two terms: a double-well potential that causes separation into two phases and an energy penalty against composition gradients that endows interfaces with tension. Two parameters of the model together specify the thickness of the interface and its interfacial tension, which can therefore be specified independently, an important advantage over the pseudopotential models described in the next section.

The distribution function $f_{k,\alpha}$ evolves according to

$$\begin{aligned} f_{k,\alpha}(\mathbf{x}_\alpha + \boldsymbol{\xi}_\alpha \Delta t, t + \Delta t) &= \\ f_{k,\alpha}(\mathbf{x}_\alpha, t) - \frac{\Delta t}{\tau_k} \left[f_{k,\alpha}(\mathbf{x}_\alpha, t) - f_{k,\alpha}^{eq}(\mathbf{x}_\alpha, t) \right] &+ \mathcal{F}_{k,\alpha} \Delta t, \end{aligned} \quad (73)$$

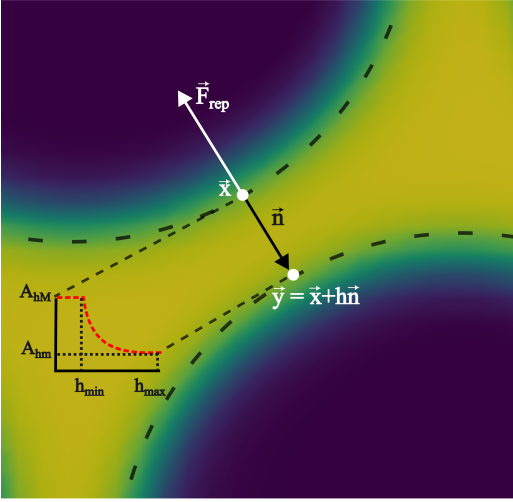


FIG. 8. Near contact forces representation. Mesoscale modelling of the interactions at the point of contact of two immiscible fluid droplets. The repulsive force is denoted by \vec{F}_{rep} , and the unit vector $\vec{n} = -\nabla\rho/|\nabla\rho|$ is perpendicular to the fluid interface. The dotted line follows the fluid interface outermost boundary, and the vectors \vec{x} and \vec{y} represent the coordinates taken there. The repulsive parameter maximum and minimum values are A_{hm} and A_{hm} , respectively. The colours represent the density field i.e. yellow is the continuum fluid and blue is the dispersed (droplets) fluid.

where τ_k specify the relaxation rates. By relating macroscopic values to the density distributions and appropriately choosing the equilibrium distributions $f_{k,\alpha}^{eq}$, the simulations model the required continuum equations. For the $f_{k,\alpha}$ field, the macroscopic density and momentum are

$$\rho_k = \sum_{\alpha=0} f_{k,\alpha}, \quad \rho_k \mathbf{u}_k = \sum_{\alpha=0} f_{k,\alpha} \xi_{\alpha}. \quad (74)$$

and the equilibrium distribution is

$$f_{k,\alpha}^{eq} = A_{\alpha} + B_{\alpha} \mathbf{u} \cdot \xi_{\alpha} + C_{\alpha} \mathbf{u} \cdot \mathbf{u} + D_{\alpha} (\mathbf{u} \cdot \xi_{\alpha})^2 + G_{\alpha,xy} \xi_{\alpha,x} \xi_{\alpha,y}, \quad (75)$$

where index notation has been used for the last term and summation over repeated xy indices is implied. The coefficients $A_{\alpha}, B_{\alpha}, C_{\alpha}, D_{\alpha}$ and G_{α} must satisfy conservation constraints, but these constraints do not determine the coefficients uniquely. It is possible to use coefficients that minimise spurious currents¹⁰¹. For a D2Q9 velocity set, the full list of coefficients is given in Ref.³⁷ and details for construction on a D3Q19 velocity set are given in Ref.¹⁰¹.

For the phase field, the scalar ϕ specifies the composition of the fluid, and it varies between -1 (continuum phase) and 1 (droplet phase). It is determined from the density distribution by

$$\phi = \sum_{k,\alpha} f_{k,\alpha}. \quad (76)$$

The continuum equation for ϕ is the Cahn-Hilliard one

$$\frac{\partial \phi}{\partial t} + \nabla \cdot (\mathbf{u} \phi) = M \nabla^2 \mu, \quad (77)$$

where M is the mobility of the chemical potential μ . This diffusivity is determined by the relaxation time τ_{ϕ} and a free parameter P according to $M = P(\tau_g - \frac{1}{2})$, while the chemical potential is determined by the free-energy of the system. The free-energy functional $\mathfrak{F}[\phi(x)]$ is¹⁰⁰

$$\mathfrak{F} = \int_V \left[\frac{1}{c_s^2} \rho \ln \rho + \frac{1}{2} \phi^2 \left(-A + \frac{B}{2} \phi^2 \right) + \frac{\kappa_{\phi}}{2} (\nabla \phi)^2 \right] dV \quad (78)$$

The first term provides an ideal gas equation of state, the second term is a double-well potential that causes phase separation with minima at compositions $\phi_0 = \pm \sqrt{\frac{A}{B}}$, and the third term sets the interfacial tension by associating an energy penalty for changes in ϕ . The parameters A and B specify the shape of the double-well potential. Two symmetrical phases with $\phi_0 = \pm 1$, are obtained when $A = B$. The magnitude of the free energy arising from concentration gradients is determined by the parameter κ_{ϕ} . The chemical potential for this free energy is

$$\mu_{\phi} = \frac{\delta \mathfrak{F}}{\delta \phi} = -A \phi + B \phi^3 - \kappa_{\phi} \nabla^2 \phi \quad (79)$$

The one-dimensional steady-state solution for ϕ between two infinite domains provides important information on the interface, specifically its characteristic thickness and excess free energy. The solution is¹⁰⁰

$$\phi(x) = \phi_0 \tanh \frac{x}{\ell_{\phi}}, \quad (80)$$

where $\ell_{\phi} = \sqrt{2\kappa_{\phi}/B}$ is the interfacial thickness of the droplets. A review of the existing models can be found in¹⁰². The free energy model is also used to study active droplets¹⁰³⁻¹⁰⁵.

Frustrated coalescence

Literature on frustrated coalescence using the free energy LBM is scarce. We present a method used by Ref.¹⁰⁶ to study the shear thinning of immiscible droplets in a 2D channel driven by flow. It tracks two fields: the phase-field variables representing each droplet's density ϕ_i where $i = 1, \dots, N$ is the number of droplets and the fluid velocity field \mathbf{u} . The free energy is given by:

$$\mathfrak{F} = \int_V \left[\frac{\alpha}{4} \sum_i^N \phi_i^2 (\phi_i - \phi_0)^2 + \frac{\kappa_{\phi}}{2} \sum_i^N (\nabla \phi_i)^2 + \varepsilon \sum_{i,j,i < j} \phi_i \phi_j \right] dV, \quad (81)$$

where the first term represents the double well potential which ensures droplet stability. It yields two minima for $\phi_i = \phi_0$ and $\phi_i = 0$, which represent the inside and outside region of the i -th droplet, respectively. The droplet deformability properties are determined by their surface tension $\Gamma = \sqrt{8\kappa_{\phi}\alpha/9}$, and can therefore be tuned by changing the value of κ_{ϕ} in Eq. (81). The parameters κ_{ϕ} and α also determine the interfacial thickness of the droplets $\ell_{\phi} = \sqrt{2\kappa_{\phi}/\alpha}$. The third, final term describes a soft repulsion pushing the droplets apart when they

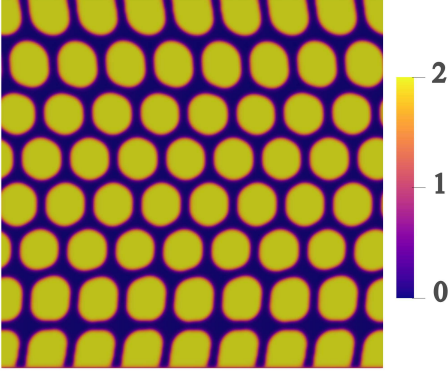


FIG. 9. Droplets moving in a channel. This was obtained using a free energy LBM and solving Eq. (82). Colour depicts $\sum_i \phi_i$ which is ≈ 2 for droplets (yellow) and ≈ 0 for the background fluid (black).

overlap, therefore preventing coalescence. The strength of this repulsion is regulated by the value of the positive constant ε . The dynamics of ϕ_i is given by

$$\frac{\partial \phi_i}{\partial t} + \nabla \cdot (\mathbf{u} \phi_i) = M \nabla^2 \mu_i, \quad (82)$$

where M is the mobility and $\mu_i = \partial \mathcal{F} / \partial \phi_i - \partial_\alpha \partial \mathcal{F} / \partial (\partial_\alpha \phi_i)$ is the chemical potential of the i -th droplet. Equations (81) and (82) are solved using a combination of the LBM (for the fluid flow) and finite differences (for the phase field) similar to Ref.^{99,107}. This may be used for a small number of droplets. As the number of times that Eqs. (81) and (82) are solved increases the computational cost rapidly as the number of droplets increases. This method is also useful to simulate droplets inside droplets¹⁰⁸.

C. Pseudopotential Method

Shan and Chen proposed two extensions of the LBM for multicomponent¹⁰⁹ and multiphase¹¹⁰ flows. These extensions are commonly referred to as pseudopotential or Shan-Chen models. The model works by introducing microscopic interactions between fluid elements which lead to phase separation. Examples of the use of multicomponent models include: droplet displacement in ducts¹¹¹ and high-density ratio multicomponent flows^{112,113}. The coexistence of multiple phases of a substance is due to effective attractive forces in the liquid phase. Similarly, different substances in a multicomponent mixture have different molecular forces. The force acts on pairs of molecules located at \mathbf{x} and $\tilde{\mathbf{x}} \neq \mathbf{x}$. It is also assumed that a higher density $\rho(\mathbf{x})$ of molecules leads to larger forces. The total force is given as an integral over all possible effective interactions as

$$\mathbf{F}(\mathbf{x}) = - \int (\tilde{\mathbf{x}} - \mathbf{x}) G(\mathbf{x}, \tilde{\mathbf{x}}) \psi(\mathbf{x}) \psi(\tilde{\mathbf{x}}) d^3 \tilde{\mathbf{x}}, \quad (83)$$

where $G(\mathbf{x}, \tilde{\mathbf{x}})$ gives the scale of the force between two fluid elements at \mathbf{x} and $\tilde{\mathbf{x}}$ and the density has been replaced by the

pseudopotential $\psi(\mathbf{x})$. Assuming nearest-neighbour interactions at the mesoscopic scale, the effective force on the k th component is expressed as

$$\mathbf{F}_k^r(\mathbf{x}) = - \psi_k(\mathbf{x}) \sum_{\tilde{k}} G_{\tilde{k}k} \sum_i w_i \psi_{\tilde{k}}(\mathbf{x} + \xi_i \Delta t) \xi_i \quad (84)$$

where $G_{\tilde{k}k}$ is a $k \times k$ matrix for the molecular interaction strength between components and its sign regulates whether the forces are attractive (negative) or repulsive (positive). Subscript r stands for repulsive. To create immiscible droplets \mathbf{F}_r^k needs to be repulsive. k and \tilde{k} are just two different components of the fluid system. For a multicomponent mixture (no multiphase), the diagonal components of the matrix are zero and $G_{AB} = G_{BA}$ for two components A and B . ψ_k is the pseudopotential (or effective density). The pseudopotential can take different forms. A commonly used form is

$$\psi_k(\mathbf{x}, t) = \rho_0 \left[1 - \exp\left(-\frac{\rho_k}{\rho_0}\right) \right], \quad (85)$$

where ρ_0 is a freely chosen reference density, usually unity. $\psi_k(\mathbf{x}, t) = \rho_k$ can also be used and it is an approximation of Eq. (85) at low-density. However, at higher densities, this assumption will lead to numerical instabilities¹¹⁴. In the absence of attraction between components, the pseudopotential can often be reduced to the physical density for simplicity. Nevertheless, using Eq. (85) instead of $\psi_k(\mathbf{x}, t) = \rho_k$ leads to improved numerical stability.

The pseudopotential model allows for multicomponent multiphase (MCMP) simulations, but, for simplicity, we do not present the variants of pseudopotential MCMP LBM. In what follows, we focus only on the multicomponent variant as it is the most widely used method for immiscible droplets. In the original multicomponent model of Shan and Chen, they proposed a simple forcing scheme for incorporating the interactions. Similar to the body force, it is also possible to incorporate the effective force of the interaction potential in the fluid velocity field. Nevertheless, for a multicomponent system, we introduce \mathbf{u}^{eq} which is a combined velocity (different from the physical velocity) of different components given by:

$$\mathbf{u}^{eq} = \frac{\sum_k \rho_k \mathbf{u}_k}{\sum_k \frac{\rho_k}{\tau_k}}, \quad (86)$$

where $\rho_k \mathbf{u}_k$ is the k th component of momentum. The barycentric velocity \mathbf{u} of the fluid mixture, i.e., the physical velocity and the total density are given by

$$\mathbf{u} = \frac{\sum_k \rho_k \mathbf{u}_k}{\rho}, \quad \rho = \sum_k \rho_k. \quad (87)$$

Also, the density and momentum of each component can be calculated using,

$$\rho_k = \sum_{\alpha=0} f_{k,\alpha}, \quad \rho_k \mathbf{u}_k = \sum_{i=0} f_{k,\alpha} \xi_\alpha + \frac{\mathbf{F}_k}{2}. \quad (88)$$

For a multi-component system, the time evolution of $f_{k,\alpha}(\mathbf{x}, t)$ is given by the discrete Boltzmann equation for each component k (similar to Eq. (7)),

$$f_{k,\alpha}(\mathbf{x}_i + \boldsymbol{\xi}_\alpha \Delta t, t + \Delta t) = f_{k,\alpha}(\mathbf{x}_i, t) - \frac{\Delta t}{\tau_k} \left[f_{k,\alpha}(\mathbf{x}_i, t) - f_{k,\alpha}^{eq}(\mathbf{x}_i, t) \right] + \mathcal{F}_{k,\alpha} \Delta t. \quad (89)$$

The equilibrium distribution is given by

$$f_{k,\alpha}^{eq} = \rho_k w_\alpha \left[1 + \frac{\mathbf{u}^{eq} \cdot \boldsymbol{\xi}_\alpha}{c_s^2} + \frac{(\mathbf{u}^{eq} \cdot \boldsymbol{\xi}_\alpha)^2}{2c_s^4} - \frac{(\mathbf{u}^{eq})^2}{2c_s^2} \right]. \quad (90)$$

The Guo forcing scheme³⁶ can be used to implement these forces acting in a fluid as it yields a viscosity-independent surface tension¹¹⁵, particularly with the frustrated coalescence mechanism described in the next section. Thus similar to Eq. (9),

$$\mathcal{F}_{k,\alpha} = \left(1 - \frac{1}{2\tau_k} \right) w_\alpha \left[\frac{\boldsymbol{\xi}_\alpha - \mathbf{u}^{eq}}{c_s^2} + \frac{(\boldsymbol{\xi}_\alpha \cdot \mathbf{u}^{eq}) \boldsymbol{\xi}_\alpha}{c_s^4} \right] \cdot \mathbf{F}_k, \quad (91)$$

where \mathbf{F}_k is the total force acting on component k . In this case $\mathbf{F}_k = \mathbf{F}_k^r$. Different forcing schemes can be used. Additionally, as shown in the next section, the frustrated coalescence mechanism can be introduced as an extra force term.

The pseudopotential model provides isotropy of the surface tension and spontaneous component separation which improves the numerical efficiency of the simulation. The method is successful because of its simplicity and flexibility in large-scale simulations of complex fluids. The implementation is relatively simple when compared to the other models reported so far. However, it also comes with some unphysical features such as a diffusing interface and spurious currents³².

Frustrated coalescence

To prevent coalescence a multi-range repulsive force is used which acts between the nearest neighbours and the next nearest neighbours^{115,116}. This force is used in addition to the repulsive component separation force \mathbf{F}_k^r . This means that in Eq. (91), $\mathbf{F}_k = \mathbf{F}_k^r + \mathbf{F}_k^c$ where \mathbf{F}_k^c is a competing force given by

$$\begin{aligned} \mathbf{F}_k^c = & -G_{k,1} \psi_k(\mathbf{x}) \sum_{i=0}^{L1} m_i \psi_k(\mathbf{x} + \boldsymbol{\xi}_i) \boldsymbol{\xi}_i \\ & - G_{k,2} \psi_k(\mathbf{x}) \sum_{j=0}^{L2} n_j \psi_k(\mathbf{x} + \boldsymbol{\zeta}_j) \boldsymbol{\zeta}_j, \end{aligned} \quad (92)$$

where $G_{k,1}$ and $G_{k,2}$ regulate the strength of force. It is a competing mechanism (superscript c) where the first term is an attractive force and the second term is a repulsive force between same components. This multi-range potential uses 2 different lattices $L1$ and $L2$. In 2D these are the D2Q9 and D2Q25¹¹⁶, respectively while in 3D they are D3Q41 for $L1$ and D3Q39 for $L2$ ¹¹⁷. In 2D, it is possible to completely separate the range of the forces i.e. the $L1$ lattice runs over only

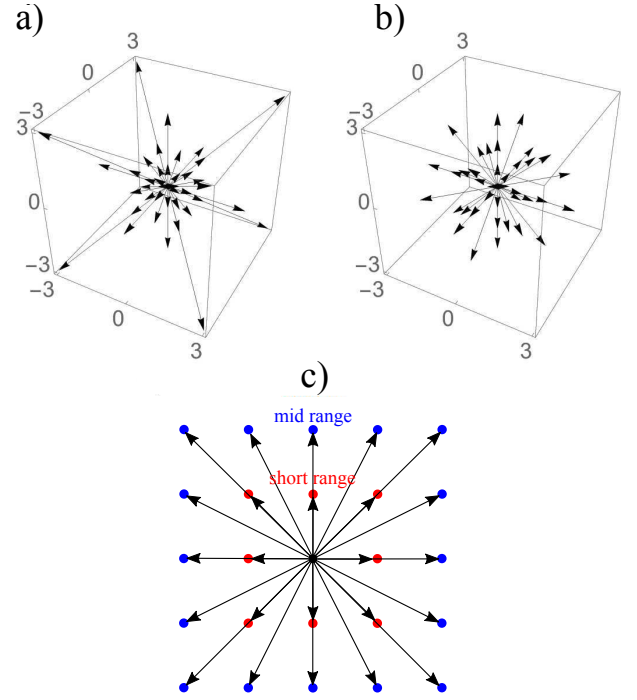


FIG. 10. (a) The D3Q41 lattice and (b) the D3Q39 lattice. The D3Q41 is a zero-one-three lattice meaning that it is analogous to the Brillouin zones (also referred to as lattice-belts, or lattice-stencils) covered by $\boldsymbol{\xi}_\alpha$. The D3Q39 is a zero-one-two-three lattice. (c) The D2Q9 lattice for short-range nodes (red). The D2Q25 lattice for short and mid-range nodes (blue).

on the first belt of neighbours while $L2$ runs over on the second belt of neighbours. However, in 3D both lattices (D3Q41 and D3Q39) run over to the third belt of neighbours but on different lattice points which is sufficient to prevent droplet coalescence¹¹⁸. In the competing force \mathbf{F}_k^c , the attractive force must overcome the repulsive force to stabilize droplets, so we set $|G_{k,1}| > |G_{k,2}|$. To obtain the desired repulsive and attractive forces: $G_{k,1} < 0$, $G_{k,2} > 0$, and $G_{k,\bar{k}} > 0$. For simplicity, we assume: $G_{A,1} = G_{B,1}$, $G_{A,2} = G_{B,2}$, $G_{A,B} = G_{B,A}$ for the two components A and B .

The computational cost does not increase with the number or size of the droplets by contrast to the colour gradient. Compared to the free energy model where each droplet is a different component, the pseudopotential model performs computationally better. This provides an efficient algorithm for simulating a large number of droplets¹¹⁹. This is because the repulsion between droplets is based on the density of each LB lattice node. The extra cost comes from using a second lattice to calculate the force. However, this model suffers from spurious velocities caused by an imbalance between the forces. Using a higher order lattice for the streaming can help to reduce these velocities¹¹⁸. These velocities increase as the viscosity ratio deviates from unity or the surface tension increase. Proper and careful calibration of the G parameters is necessary otherwise the droplet may increase or decrease in size. With this method, it is not possible to vary the surface tension and the interface thickness independently.

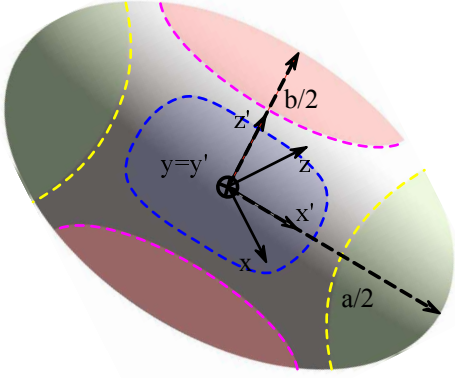


FIG. 11. The final steady-state shape of droplet/capsule with the major axis, a , the minor axis of deformation, b , and the third axis, c . An additional reference frame (x', y', z') is defined, with the axes corresponding to the deformed droplet principal axes. The different regions of the droplet have been also highlighted for ease of reference: tips (green), belly (red) and sides (blue).

V. BENCHMARKS

We now summarise a few simple benchmarks that can be used to test the model implementation in hydrostatic and hydrodynamic conditions. The benchmarks are for one capsule/droplet in shear flow, capsule sedimentation and a test of the Laplace law. We refer the reader to Ref.¹¹⁵ for benchmarks on multiple droplets.

A. Capsule and droplet in shear flow

Shear flow is a common validation flow to test for both droplets^{120,121} and capsules^{85,122} (fluid-structure interactions). Here we use capsules as a generic term for membrane-bound particles. This benchmark consists of placing a spherical (circular in 2D) droplet/capsule in shear flow (between two parallel walls with opposite velocities) and allowing it to deform until a steady state regime is reached (see Fig. 11). In what follows, we have separated into two subsections the shear flow of a droplet and a capsule for clarity.

1. Droplet

As a droplet deforms in shear flow, the final shape is a result of viscous forces competing with surface tension. The ratio of these forces is the Capillary number,

$$\text{Ca} = \frac{u_w \mu}{\Gamma} \frac{R}{H}, \quad (93)$$

where u_w is the wall velocity, H is the distance between walls, R is the radius of the droplet, μ the dynamic viscosity and Γ is the surface tension. Ca is the main parameter that controls the deformation and final shape of the droplet. The final shape is

evaluated using the Taylor deformation parameter given by

$$D = \frac{a - b}{a + b} \quad (94)$$

where a and b are the lengths of the major and minor axis, respectively. In the limit of small Capillary numbers (thus small deformations) a steady state is always achieved. In the limit of nearly spherical droplets an analytical solution was first reported in Ref.¹²³ by solving the momentum and continuity equation using the Lorentz reflection method. Reference¹²³ gives the first order solution D_{SH} (SH stands for the initials of the original authors in Ref.¹²³) for small confinements ratio R/H between two parallel walls^{123,124}

$$D_{SH} = D_{Taylor} \left[1 + C_{SH} \frac{1 + 2.5p}{1 + p} \left(\frac{R}{H} \right)^3 \right], \quad (95)$$

where p is the viscosity ratio between the droplet and surrounding fluid, H is the gap between the walls, R is the droplet radius and parameter C_{SH} which depends on the position of the droplet relative to the walls and this value grows when closer to the walls. Reference¹²³ performed experiments for which they found a droplet placed in the middle of the walls ($R/H = 0.5$) has $C_{SH} = 5.699$ while a droplet at $R/H = 0.125$ has $C_{SH} = 193.3$. Other values at different droplet positions are also presented. The theoretical model given Eq. (95) and Ref.¹²³ has an additional term D_{Taylor} obtained from Taylor small-deformation bulk theory^{125,126} and is given by

$$D_{Taylor} = \text{Ca} \frac{16 + 19p}{8(1 + p)} \sin \theta \cos \theta, \quad (96)$$

where Ca is the Capillary number and θ is the angle between reference axis x and major axis a (see Fig. 11) and usually assumed to be $\pi/4$ radians as in Ref.^{124,125}. Taylor bulk theory^{125,126} is valid for small deformations and viscosity ratios p close to 1. Furthermore, while this theoretical model predicts that the magnitude of the deformation will scale with the confinement ratio, the shape should remain ellipsoidal.

We highlight that this test can be performed in both 2D and 3D for droplets. For small Ca the deformation parameter is the same for a 2D and 3D droplet (same parameters), while for higher Ca results for 2D and 3D droplets start to deviate. An extensive study of 2D vs 3D droplets can be found in Ref.¹²⁷. The methodology presented here is valid for all the fluid-fluid models mentioned in this review.

2. Capsule

A capsule in shear will also reach a steady state and the main parameter defining the deformation is also the Capillary number now defined as $\text{Ca} = \frac{u_w R \mu}{k_s H}$ where k_s is the stretching coefficient and has the same physical units as the surface tension Γ . The Taylor deformation parameter is also used to characterise capsules in shear flow. We highlight that the correct constitutive model needs to be used to compare with other literature or analytical results. Results and validation for

Hookean constitutive laws can be found in Ref.^{128–130}. For Skalak models we refer the reader to Ref.^{10,131,132}. It is not trivial to obtain analytical results from constitutive models. In most cases, models are validated against other numerical implementations. An analytical result for the Taylor deformation parameter has been found for the neo-Hookean and Skalak laws, Eqs (12) and (14) and is given by^{10,133,134},

$$D = \frac{5}{4} \frac{3\alpha_2 + 4\alpha_3}{\alpha_1(3\alpha_2 + 5\alpha_3) + 2\alpha_3(\alpha_2 + \alpha_3)} \text{Ca} + O(\text{Ca}^2) \quad (97)$$

where $\alpha_1 = 0$, $\alpha_2 = 2/3$, and $\alpha_3 = 1/3$ are coefficients extracted from the constitutive model. Equation (97) is only valid for small deformation in Stokes flow ($\text{Re} < 1$). More details can be found in Ref.¹⁰

B. Capsule sedimentation

The process of capsule sedimentation involves placing a capsule in a static fluid and allowing it to accelerate downward under gravity until it reaches a terminal velocity, where the resultant drag force balances the gravitational load (see Fig. 12). We present a simple validation for a confined 2D capsule using the harmonic potential given in Eq. (32). The capsule should be rigid. The elastic and bending coefficients can be adjusted to achieve a quasi-rigid state. It is clear that simulating sedimentation of a 2D capsule i.e. a cylinder, will encounter Stokes' paradox, which states that there is no drag force on the cylinder in the Stokes regime. However, experiments and approximations have been derived for cylinder sedimentation in the presence of walls. Therefore, this benchmark consists of placing the 2D capsule between 2 vertical parallel walls. The top and bottom boundaries can be walls or periodic but the vertical walls need to be long enough to minimize boundary effects.

According to Ref.¹³⁵, the analytical wall-corrected settling velocity of a 2D particle can be calculated from

$$V_c = \frac{\pi g D^2 (\rho_s - \rho_f)}{4\mu\Lambda}, \quad (98)$$

where D is the diameter of the particle, g is gravitational acceleration, ρ is the density where s and f stand for solid and fluid, respectively, μ is the dynamic viscosity and Λ is the wall correction factor. Subscript c stands for corrected. Notice that Eq. (98) is obtained by equating the gravitational force per unit length $F_g = \frac{\pi}{4} g D^2 (\rho_s - \rho_f)$ with the drag force per unit length $F_d = V_c \mu \Lambda$. Moreover, Eq. (98) is valid for low Reynolds numbers. There are several approximations for Λ which can be found in Ref.^{135,136}. A commonly cited approximation can be found in Ref.^{137,138} where Stokes equation for Newtonian fluids using asymptotic expansion with no-slip boundary conditions on the walls given by

$$\Lambda = \frac{-4\pi}{0.9157 + \ln(k) - 1.724k^2 + 1.730k^4 - 2.406k^6 + 4.591k^8} \quad (99)$$

where $k = D/H$ is the dimensionless particle size. D is the diameter of the particle and H is the distance between the two

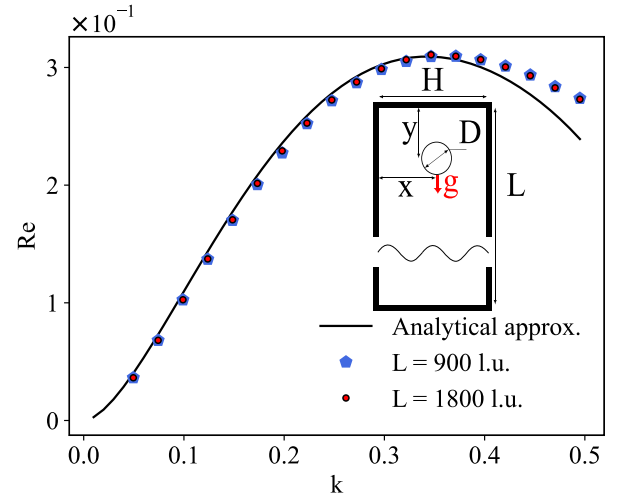


FIG. 12. (a) Schematic of an initially circular particle of diameter D moving in a channel of length L and width H due to the force of gravity g . The particle is placed at $x_0 = 0.5H$. (b) Terminal velocity V_t against dimensionless size k . The particle has a diameter of 12.5 l.u and the fluid has a relaxation parameter $\tau = 1$. The analytical approximation corresponds to Eq. (98).

vertical walls i.e., the width of the channel. Reference^{137,138} applied an integral transform which produces a convergent series and allows the boundary conditions to be applied simultaneously. It is generally known that Eq. (99) is valid for $k \in [0, 0.5]$. Usually, Λ is only a function of k for low or very high Reynolds numbers Re . For intermediate values, it is also a function of the Reynolds number. The results for a 2D sedimenting capsule are shown in Fig. 12 and are in agreement up to $k \approx 0.4$ in the range $k \in [0, 0.5]$. Note that for a 3D spherical capsule, Stokes' law can be used for validation.

C. Droplet Laplace test

The Laplace test consists of placing a spherical droplet in the centre of a fluid domain and verifying the Laplace law. Laplace law dictates that when the system reaches equilibrium, the pressure difference across the droplet interface ΔP is related to the interfacial tension Γ

$$\Delta P = \frac{2\Gamma}{R}, \quad (100)$$

where R is the radius of the droplet. In 2D the Laplace pressure is $\Delta P = \frac{\Gamma}{R}$. One should measure the pressure at the droplet centre and then as far away from the centre as possible to prevent undesired effects from affecting the measurements such as spurious velocities. The domain needs to be large enough to prevent the effect of periodic copies (periodic boundaries) or walls (solid boundaries). A linear relationship should be obtained and the slope is the surface tension. As an example, we plot results for a droplet using the pseudopotential method depicted in Fig. 13. Additionally, it is possible to

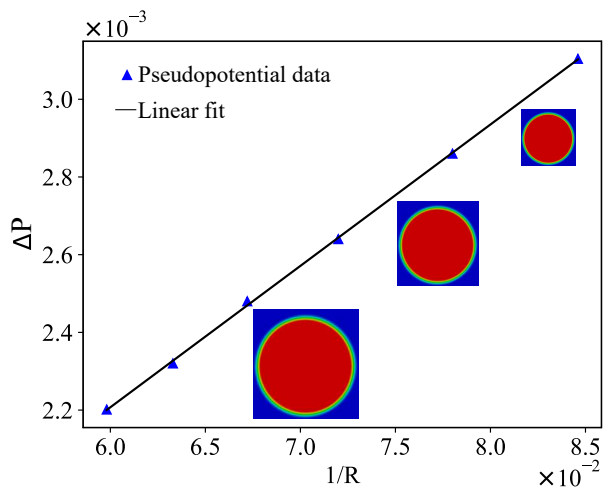


FIG. 13. Laplace test using the pseudopotential method at equilibrium for $G_{k,1} = -7.9$, $G_{k,2} = 4.9$ (see Eq. (92)) and $\tau_A = \tau_B = 1$. From the linear fit we obtain the surface tension $\Gamma = 0.00367$. The images show the steady state of droplets as we vary the radius.

compare the surface tension value to theoretical and numerical values¹³⁹. Moreover, other hydrostatic tests such as contact angle test¹³⁹ (for wetting boundary conditions) can be useful to further check the accuracy of the model.

VI. SUMMARY AND OUTLOOK

We reviewed different methods to model fluid-filled objects in flow and addressed some of the advantages, disadvantages, and trade-offs of the different methodologies, as perceived based on our own (necessarily biased) experience and the literature survey. Below, we summarise the main items.

Fluid-fluid models are usually computationally more economical than fluid-structure ones because the interfaces emerge spontaneously from the underlying mesoscale physics and do not require any explicit tracking. The price for this flexibility is a lack of specific control of the mechanical properties of the interfaces, as often required in biological applications. They are also generally affected by spurious currents resulting from lack of sufficient isotropy of the underlying lattice; even though several efficient remedies have been developed over the years, spurious currents remain an issue to be critically monitored.

Both pseudo-potential and free energy must be supplemented with a model for near-contact interactions in order to prevent droplet coalescence, especially under conditions typical of microfluidic experiments. Such near-contact interactions can be implemented very effectively within high-performance LB codes, yielding excellent performances on parallel GPU clusters. For instance, optimized codes running on GPU accelerators can reach GLUPS performance (one billion lattice updates per second) on single GPU machines with a few thousands CUDA cores^{140,141}. To convey a concrete idea means that one can simulate one millimeter cube mate-

rial at micron resolution in space and nanosecond resolution in time, over one millisecond timespan in about 10^6 seconds, namely about two weeks wall clock time. On massively parallel GPU clusters, these figures can be boosted by two orders of magnitude, meaning that the above simulation can be performed in just a few hours of wall-clock time. These numbers open up exciting perspectives for the computational design of new soft materials^{16,142}. Fluid-fluid models readily extend to three dimensions by simply enlarging the set of discrete velocities, although at a correspondingly increased computational cost (especially on account of memory access)¹⁴³.

As mentioned above, fluid-structure models are computationally intensive but offer a more accurate control of the mechanical properties of the interfaces, hence of the shape of the resulting droplets and capsules. They also provide a significant latitude in shape-space and do not suffer from significant spurious current effects. Since the structural dynamics is explicitly taken into account, the computational cost raises with the number of droplets and the number of degrees of freedom per droplet/capsule, setting the case for a judicious trade-off between physical fidelity and computational viability. Significant progress over the recent years has led to near-GLUPS performance on multi-million grid sizes with embedded propellers¹⁴⁴.

Finally, three-dimensional extensions are demanding not only in terms of computational resources, but also in terms of model and programming complexity, such as the switch to finite-element representations of the internal degrees of freedom.

By and large, it appears fair to say that the major progress of LB models over the last decade, both in its fluid-fluid and fluid-structure versions has come to a point of enabling the computational study of new smart materials, both passive and active. Furthermore, the capability of tracking droplets and capsules in realistically complex geometries, such as the human body, may disclose new exciting perspectives in computational microphysiology and medicine¹⁴⁵.

ACKNOWLEDGEMENTS

We acknowledge financial support from the Portuguese Foundation for Science and Technology (FCT) under the contracts: PTDC/FIS-MAC/28146/2017 (LISBOA-01-0145-FEDER-028146), EXPL/FIS-MAC/0406/2021, UIDB/00618/2020, UIDP/00618/2020 and 2020.08525.BD. SS wishes to acknowledge financial support from the ERC-PoC grants DROPTRACK (contract number 101081171).

¹S. L. Anna and H. C. Mayer, *Physics of Fluids* **18**, 121512 (2006).

²H. Liu and Y. Zhang, *Physics of Fluids* **23**, 082101 (2011).

³J. R. Clausen and C. K. Aidun, *Physics of Fluids* **22**, 123302 (2010).

⁴Y. Sui, Y. T. Chew, and H. T. Low, *International Journal of Modern Physics C* **18**, 993–1011 (2007).

⁵C. K. Aidun and J. R. Clausen, *Annual Review of Fluid Mechanics* **42**, 439 (2010).

⁶R. Benzi, S. Succi, and M. Vergassola, *Physics Reports* **222**, 145 (1992), ISSN 0370-1573.

⁷T. Ye, D. Pan, C. Huang, and M. Liu, *Physics of Fluids* **31**, 011301 (2019).

- ⁸H. Zhu, Z. Zhou, R. Yang, and A. Yu, *Chemical Engineering Science* **63**, 5728–5770 (2008).
- ⁹T. Gao and H. H. Hu, *Journal of Computational Physics* **228**, 2132–2151 (2009).
- ¹⁰T. Krüger, F. Varnik, and D. Raabe, *Computers and Mathematics with Applications* **61**, 3485 (2011), ISSN 0898-1221.
- ¹¹K. Sugiyama, S. Ii, S. Takeuchi, S. Takagi, and Y. Matsumoto, *Computational Mechanics* **46**, 147–157 (2010).
- ¹²W. Gao and Y. Chen, *International Journal of Heat and Mass Transfer* **135**, 158–163 (2019).
- ¹³G. Hou, J. Wang, and A. Layton, *Communications in Computational Physics* **12**, 337–377 (2012).
- ¹⁴U. D. Schiller, T. Krüger, and O. Henrich, *Soft Matter* **14**, 9–26 (2018).
- ¹⁵S. Karimnejad, A. A. Delouei, H. Başağaoğlu, M. Nazari, M. Shahmardan, G. Falcucci, M. Lauricella, and S. Succi, *Communications in Computational Physics* **32**, 899 (2022).
- ¹⁶S. Succi, *The Lattice Boltzmann Equation: For Complex States of Flowing Matter* (Oxford University Press, 2018).
- ¹⁷T. Krüger, H. Kusumaatmaja, A. Kuzmin, O. Shardt, G. Silva, and E. M. Viggen, *The Lattice Boltzmann Method* (Springer International Publishing, 2017).
- ¹⁸M. L. Manning, *Phys. Rev. Lett.* **130**, 130002 (2023).
- ¹⁹R. C. V. Coelho, N. A. M. Araújo, and M. M. Telo da Gama, *Soft Matter* **18**, 7642 (2022).
- ²⁰A. Be'er and G. Ariel, *Movement Ecology* **7** (2019).
- ²¹B. Dunweg and A. J. C. Ladd, in *Advanced Computer Simulation Approaches for Soft Matter Sciences III* (Springer Berlin Heidelberg, 2009), pp. 89–166.
- ²²U. Frisch, B. Hasslacher, and Y. Pomeau, *Physical Review Letters* **56**, 1505 (1986).
- ²³Y. H. Qian, D. D’Humières, and P. Lallemand, *Europhysics Letters* **17**, 479 (1992), ISSN 0295-5075.
- ²⁴X. He and L.-S. Luo, *Journal of Statistical Physics* **88**, 927 (1997), ISSN 1572-9613.
- ²⁵A. K. Gunstensen, D. H. Rothman, S. Zaleski, and G. Zanetti, *Physical Review A* **43**, 4320 (1991).
- ²⁶S. Chen and G. D. Doolen, *Annual Review of Fluid Mechanics* **30**, 329 (1998).
- ²⁷S. Succi, *The Lattice Boltzmann Equation: For Fluid Dynamics and Beyond* (Oxford Science Publications, 2001).
- ²⁸A. J. C. Ladd, *Journal of Fluid Mechanics* **271**, 311 (1994), ISSN 1469-7645, 0022-1120.
- ²⁹X. He, S. Chen, and R. Zhang, *Journal of Computational Physics* **152**, 642–663 (1999).
- ³⁰A. Cali, S. Succi, A. Cancelliere, R. Benzi, and M. Gramignani, *Phys. Rev. A* **45**, 5771 (1992).
- ³¹X. He, S. Chen, and G. D. Doolen, *Journal of Computational Physics* **146**, 282 (1998), ISSN 0021-9991.
- ³²T. Krüger, H. Kusumaatmaja, A. Kuzmin, O. Shardt, G. Silva, and E. M. Viggen, *The Lattice Boltzmann Method*, Graduate Texts in Physics (Springer International Publishing, 2017).
- ³³S. A. Bawazeer, S. S. Baakeem, and A. A. Mohamad, *Archives of Computational Methods in Engineering* **28**, 4405 (2021), ISSN 1886-1784.
- ³⁴K. Sun, T. Wang, M. Jia, and G. Xiao, *Physica A Statistical Mechanics and its Applications* **391**, 3895 (2012).
- ³⁵L. Chen, Q. Kang, Y. Mu, Y.-L. He, and W.-Q. Tao, *International Journal of Heat and Mass Transfer* **76**, 210 (2014).
- ³⁶Z. Guo, C. Zheng, and B. Shi, *Physical Review* **65**, 046308 (2002).
- ³⁷H. Huang, M. C. Sukop, and X.-Y. Lu, *Multiphase lattice Boltzmann methods: theory and application* (John Wiley and Sons, Inc, Chichester, West Sussex, 2015).
- ³⁸W. Lei, C. Xie, T. Wu, X. Wu, and M. Wang, *Sci Rep* **9**, 1453 (2019), ISSN 2045-2322.
- ³⁹J. Zhang, P. C. Johnson, and A. S. Popel, *Phys. Biol.* **4**, 285 (2007), ISSN 1478-3975.
- ⁴⁰W. R. Dodson and P. Dimitrakopoulos, *Journal of Fluid Mechanics* **641**, 263–296 (2009).
- ⁴¹Y. Imai, T. Omori, Y. Shimogonya, T. Yamaguchi, and T. Ishikawa, *Journal of Biomechanics* **49**, 2221–2228 (2016).
- ⁴²T. M. Fischer, *Biophysical Journal* **86**, 3304–3313 (2004).
- ⁴³T. Omori, T. Ishikawa, D. Barthès-Biesel, A.-V. Salsac, J. Walter, Y. Imai, and T. Yamaguchi, *Physical Review E* **83**, 041918 (2011).
- ⁴⁴D.-K. Sun and Z. Bo, *International Journal of Heat and Mass Transfer* **80**, 139–149 (2015).
- ⁴⁵D. C. Bottino, *Journal of Computational Physics* **147**, 86–113 (1998).
- ⁴⁶C. S. Peskin, *Acta Numerica* **11**, 479–517 (2002).
- ⁴⁷J. M. Charrier, S. Shrivastava, and R. Wu, *The Journal of Strain Analysis for Engineering Design* **24**, 55 (1989), ISSN 0309-3247, publisher: IMECHE.
- ⁴⁸S. Shrivastava and J. Tang, *The Journal of Strain Analysis for Engineering Design* **28**, 31 (1993), ISSN 0309-3247, 2041-3130.
- ⁴⁹T. Krüger, *Computer Simulation Study of Collective Phenomena in Dense Suspensions of Red Blood Cells under Shear* (Vieweg+Teubner Verlag, 2012).
- ⁵⁰D. Barthès-Biesel, A. Diaz, and E. Dhenin, *Journal of Fluid Mechanics* **460**, 211 (2002), ISSN 0022-1120, 1469-7645.
- ⁵¹S. Ramanujan and C. Pozrikidis, *Journal of Fluid Mechanics* **361**, 117 (1998), ISSN 0022-1120, 1469-7645.
- ⁵²R. Skalak, A. Tozeren, R. P. Zarda, and S. Chien, *Biophysical Journal* **13**, 245 (1973), ISSN 0006-3495.
- ⁵³Y. Sui, Y. T. Chew, P. Roy, Y. P. Cheng, and H. T. Low, *Physics of Fluids* **20**, 112106 (2008), ISSN 1070-6631.
- ⁵⁴K. Vahidkhal, S. L. Diamond, and P. Bagchi, *Biophysical Journal* **106**, 2529–2540 (2014).
- ⁵⁵A. Guckenberger, M. P. Schraml, P. G. Chen, M. Leonetti, and S. Gekle, *Computer Physics Communications* **207**, 1 (2016), ISSN 00104655.
- ⁵⁶A. Guckenberger and S. Gekle, *Journal of Physics: Condensed Matter* **29**, 203001 (2017), ISSN 0953-8984, 1361-648X.
- ⁵⁷W. Helfrich, *Zeitschrift für Naturforschung C* **28**, 693 (1973), ISSN 1865-7125, 0939-5075.
- ⁵⁸O.-Y. Zhong-can and W. Helfrich, *Physical Review A* **39**, 5280 (1989), ISSN 0556-2791.
- ⁵⁹K. Sinha and M. D. Graham, *Physical Review E* **92**, 042710 (2015), ISSN 1539-3755, 1550-2376.
- ⁶⁰M. Reuter, S. Biasotti, D. Giorgi, G. Patanè, and M. Spagnuolo, *Computers & Graphics* **33**, 381 (2009), ISSN 00978493.
- ⁶¹Cha Zhang and Tsuhan Chen, in *Proceedings 2001 International Conference on Image Processing (Cat. No.01CH37205)* (IEEE, Thessaloniki, Greece, 2001), vol. 2, pp. 935–938.
- ⁶²Z. Gou, X. Ruan, F. Huang, and X. Fu, *Computer Methods in Biomechanics and Biomedical Engineering* **22**, 465 (2019), ISSN 1025-5842, 1476-8259.
- ⁶³J. Li, G. Lykotrafitis, M. Dao, and S. Suresh, *Proceedings of the National Academy of Sciences* **104**, 4937 (2007), ISSN 0027-8424.
- ⁶⁴G. E. K. D. A. Fedosov, B. Caswell, *Biophysical Journal* **98**, 2215 (2010), ISSN 0006-3495.
- ⁶⁵K. ichi Tsubota, S. Wada, and T. Yamaguchi, *Computer Methods and Programs in Biomedicine* **83**, 139 (2006), ISSN 0169-2607.
- ⁶⁶C. Pozrikidis, *Computational hydrodynamics of capsules and biological cells* (CRC Press, 2010).
- ⁶⁷T. Wu and J. J. Feng, *Biomicrofluidics* **7**, 044115 (2013), ISSN 1932-1058.
- ⁶⁸M. Nakamura, S. Bessho, and S. Wada, *International Journal for Numerical Methods in Biomedical Engineering* **29**, 114 (2013), ISSN 2040-7947.
- ⁶⁹M. Nakamura, S. Bessho, and S. Wada, *International Journal for Numerical Methods in Biomedical Engineering* **30**, 42 (2014), ISSN 2040-7947.
- ⁷⁰C. W. Hirt, A. A. Amsden, and J. L. Cook, *Journal of Computational Physics* **14**, 227 (1974), ISSN 0021-9991.
- ⁷¹S. Kollmannsberger, S. Geller, A. Düster, J. Tölke, C. Sorger, M. Krafczyk, and E. Rank, *International Journal for Numerical Methods in Engineering* **79**, 817 (2009), ISSN 00295981, 10970207.
- ⁷²P. Ahrlichs and B. Dünweg, *International Journal of Modern Physics C* **09**, 1429 (1998), ISSN 0129-1831, 1793-6586.
- ⁷³P. Ahrlichs and B. Dünweg, *The Journal of Chemical Physics* **111**, 8225 (1999), ISSN 0021-9606, 1089-7690.
- ⁷⁴C. W. Hsu and Y.-L. Chen, *Journal of Chemical Physics* **133**, 034906 (2010), ISSN 0021-9606.
- ⁷⁵G. Herschlag and L. Miller, *Journal of Theoretical Biology* **285**, 84 (2011), ISSN 0022-5193.
- ⁷⁶J. Zhang, P. C. Johnson, and A. S. Popel, *Journal of Biomechanics* **41**, 47 (2008), ISSN 0021-9290.

- ⁷⁷Y. Liu and W. K. Liu, *Journal of Computational Physics* **220**, 139 (2006), ISSN 0021-9991.
- ⁷⁸L. M. Cowl and A. L. Fogelson, *International Journal for Numerical Methods in Biomedical Engineering* **26**, 471 (2010), ISSN 2040-7947.
- ⁷⁹R. Mittal and G. Iaccarino, *Annual Review of Fluid Mechanics* **37**, 239 (2005).
- ⁸⁰A. J. C. Ladd and R. Verberg, *Journal of Statistical Physics* **104**, 1191 (2001), ISSN 1572-9613.
- ⁸¹A. J. C. Ladd, *Physics of Fluids* **9**, 491 (1997), ISSN 1070-6631.
- ⁸²A. S. Nunes, R. C. V. Coelho, V. C. Braz, M. M. Telo da Gama, and N. A. M. Araújo, *Communications in Computational Physics* **33**, 1 (2023), ISSN 1815-2406, 1991-7120.
- ⁸³M. Gross, T. Krueger, and F. Varnik, *Soft Matter* **10**, 4360 (2014).
- ⁸⁴Y. Kwon, *Engineering Computations* **23**, 860 (2006), ISSN 0264-4401.
- ⁸⁵R. M. MacMECCAN, J. R. Clausen, G. P. Neitzel, and C. K. Aidun, *Journal of Fluid Mechanics* **618**, 13 (2009), ISSN 0022-1120, 1469-7645.
- ⁸⁶T. Krüger, F. Varnik, and D. Raabe, *Physical Review E* **79**, 046704 (2009).
- ⁸⁷B. Dünweg and A. J. C. Ladd, in *Advanced Computer Simulation Approaches for Soft Matter Sciences III* (Springer Berlin Heidelberg, Berlin, Heidelberg, 2009).
- ⁸⁸D. Rothman and J. Keller, *Journal of Statistical Physics* **52**, 1119–1127 (1988).
- ⁸⁹A. Gunstensen, D. Rothman, S. Zaleski, and G. Zanetti, *Physical Review A* **43**, 4320 (1991).
- ⁹⁰D. Grunau, S. Chen, and K. Eggert, *Physics of Fluids A* **5**, 2557 (1993).
- ⁹¹M. Latva-Kokko and D. Rothman, *Physical Review* **71**, 056702 (2005).
- ⁹²S. Leclaire, M. Reggio, and J.-Y. Trépanier, *Applied Mathematical Modelling* **36**, 2237–2252 (2012).
- ⁹³H. Liu, A. Valocchi, and Q. Kang, *Physical Review* **85**, 046309 (2012).
- ⁹⁴T. Reis and T. N. Phillips, *Journal of Physics A: Mathematical and Theoretical* **40**, 4033–4053 (2007).
- ⁹⁵S. Leclaire, A. Parmigiani, O. Malaspinas, B. Chopard, and J. Latt, *Physical Review E* **95**, 033306 (2017).
- ⁹⁶A. Montessori, M. Lauricella, and S. Succi, *Philosophical Transactions of the Royal Society A: Mathematical, Physical and Engineering Sciences* **377**, 20180149 (2019).
- ⁹⁷A. Montessori, M. Lauricella, N. Tirelli, and S. Succi, *Journal of Fluid Mechanics* **872**, 327–347 (2019).
- ⁹⁸A. Montessori, A. Tiribocchi, F. Bonaccorso, M. Lauricella, and S. Succi, *Philosophical Transactions of the Royal Society A: Mathematical, Physical and Engineering Sciences* **378**, 20190406 (2020).
- ⁹⁹M. Swift, E. Orlandini, W. Osborn, and J. Yeomans, *Physical Review* **54**, 5041–5052 (1996).
- ¹⁰⁰A. J. Briant and J. M. Yeomans, *Physical Review E* **69**, 031603 (2004).
- ¹⁰¹C. M. Pooley and K. Furtado, *Physical Review E* **77**, 046702 (2008).
- ¹⁰²X. He and G. Doolen, *Journal of Statistical Physics* **107**, 309–328 (2002).
- ¹⁰³A. Tiribocchi, M. Durve, M. Lauricella, A. Montessori, D. Marenduzzo, and S. Succi, *Nature Communications* **14**, 1096 (2023).
- ¹⁰⁴R. C. V. Coelho, N. A. M. Araújo, and M. M. Telo da Gama, *Philosophical Transactions of the Royal Society A: Mathematical, Physical and Engineering Sciences* **379**, 20200394 (2021).
- ¹⁰⁵R. C. V. Coelho, H. R. J. C. Figueiredo, and M. M. Telo da Gama, *Phys. Rev. Res.* **5**, 033165 (2023).
- ¹⁰⁶M. Fogliano, A. Morozov, O. Henrich, and D. Marenduzzo, *Physical Review Letters* **119**, 208002 (2017).
- ¹⁰⁷A. Tiribocchi, N. Stella, G. Gonnella, and A. Lamura, *Physical Review E* **80**, 026701 (2009).
- ¹⁰⁸A. Tiribocchi, A. Montessori, M. Lauricella, F. Bonaccorso, S. Succi, S. Aime, M. Milani, and D. A. Weitz, *Nature Communications* **12**, 82 (2021).
- ¹⁰⁹X. Shan and H. Chen, *Physical Review* **47**, 1815–1815 (1993).
- ¹¹⁰X. Shan and H. Chen, *Physical Review* **49**, 2941 (1994).
- ¹¹¹Q. Kang, D. Zhang, and S. Chen, *Journal of Fluid Mechanics* **545**, 41–66 (2005).
- ¹¹²J. Bao and L. Schaefer, *Applied Mathematical Modelling* **37**, 1860–1871 (2013).
- ¹¹³C. Stiles and Y. Xue, *Computers & Fluids* **131**, 81–90 (2016).
- ¹¹⁴M. Sbragaglia, R. Benzi, L. Biferale, S. Succi, K. Sugiyama, and F. Toschi, *Physical Review* **75**, 026702 (2007).
- ¹¹⁵L. Fei, A. Scagliarini, A. Montessori, M. Lauricella, S. Succi, and K. H. Luo, *Physical Review Fluids* **3**, 104304 (2018).
- ¹¹⁶R. Benzi, M. Sbragaglia, A. Scagliarini, P. Perlekar, M. Bernaschi, S. Succi, and F. Toschi, *Soft Matter* **11**, 1271–1280 (2015).
- ¹¹⁷S. S. Chikatamarla and I. V. Karlin, *Phys. Rev. E* **79**, 046701 (2009).
- ¹¹⁸D. P. F. Silva, R. C. V. Coelho, M. M. T. da Gama, and N. A. M. Araújo, *Physical Review E* **107**, 035106 (2023).
- ¹¹⁹R. C. V. Coelho, D. P. F. Silva, A. M. R. Maschio, M. M. Telo da Gama, and N. A. M. Araújo, *Physics of Fluids* **35**, 013304 (2023).
- ¹²⁰A. Yiotis, J. Psihogios, M. Kainourgiakis, A. Papaioannou, and A. Stubos, *Colloids and Surfaces A: Physicochemical and Engineering Aspects* **300**, 35–49 (2007).
- ¹²¹G. Soligo, A. Roccon, and A. Soldati, *Meccanica* **55**, 371–386 (2020).
- ¹²²C. D. Eggleton and A. S. Popel, *Physics of Fluids* **10**, 1834–1845 (1998).
- ¹²³M. Shapira and S. Haber, *International Journal of Multiphase Flow* **16**, 305–321 (1990).
- ¹²⁴A. Vananroye, P. Puyvelde, and P. Moldenaers, *Journal of Rheology* **51**, 139–153 (2007).
- ¹²⁵G. Taylor, *Proceedings of the Royal Society of London. Series A, Containing Papers of a Mathematical and Physical Character* **138**, 41–48 (1932).
- ¹²⁶G. Taylor, *Proceedings of the Royal Society of London A: Mathematical, Physical and Engineering Sciences* **146**, 501–523 (1934).
- ¹²⁷S. Afkhami, P. Yue, and Y. Renardy, *Physics of Fluids* **21**, 072106 (2009).
- ¹²⁸Z. Gou, F. Huang, X. Ruan, and X. Fu, *Communications in Computational Physics* **24** (2018).
- ¹²⁹A. Rahmat, J. Meng, D. R. Emerson, C.-Y. Wu, M. Barigou, and A. Alexiadis, *Microfluidics and Nanofluidics* **25**, 1 (2021).
- ¹³⁰Y. Sui, Y. T. Chew, P. Roy, X. B. Chen, and H. T. Low, *Physical Review E* **75**, 066301 (2007).
- ¹³¹M. Wouters, O. Aouane, T. Krüger, and J. Harting, *Physical Review E* **100**, 033309 (2019).
- ¹³²F. Guglietta, M. Behr, L. Biferale, G. Falcucci, and M. Sbragaglia, *Soft Matter* **16**, 6191–6205 (2020).
- ¹³³D. Barthès-Biesel, *Journal of Fluid Mechanics* **100**, 831–853 (1980).
- ¹³⁴D. Barthès-Biesel and J. M. Rallison, *Journal of Fluid Mechanics* **113**, 251 (1981).
- ¹³⁵S. Ghosh and J. M. Stockie, *Communications in Computational Physics* **18**, 380–416 (2015).
- ¹³⁶A. Ben Richou, A. Ambari, M. Lebey, and J. Naciri, *Chemical Engineering Science* **60**, 2535 (2005), ISSN 00092509.
- ¹³⁷O. H. Faxen, *Proceedings of the Royal Swedish Academy of Sciences* **187**, 1 (1946).
- ¹³⁸J. Happel and H. Brenner, *Low Reynolds number hydrodynamics: with special applications to particulate media*, no. v. 1 in *Mechanics of fluids and transport processes* (Springer, 1983), 1st ed.
- ¹³⁹E. Montellà, B. Chareyre, S. Salager, and A. Gens, *MethodsX* **7**, 101090 (2020).
- ¹⁴⁰F. Bonaccorso, M. Lauricella, A. Montessori, G. Amati, M. Bernaschi, F. Spiga, A. Tiribocchi, and S. Succi, *Computer Physics Communications* **277**, 108380 (2022), ISSN 0010-4655.
- ¹⁴¹A. Tiribocchi, A. Montessori, G. Amati, M. Bernaschi, F. Bonaccorso, S. Orlandini, S. Succi, and M. Lauricella, *The Journal of Chemical Physics* **158**, 104101 (2023), ISSN 0021-9606.
- ¹⁴²S. Succi, G. Amati, M. Bernaschi, G. Falcucci, M. Lauricella, and A. Montessori, *Computers & Fluids* **181**, 107 (2019), ISSN 0045-7930.
- ¹⁴³G. Falcucci, G. Amati, P. Fanelli, V. K. Krastev, G. Polverino, M. Porfiri, and S. Succi, *Nature* **595**, 537 (2021).
- ¹⁴⁴J. Latt, O. Malaspinas, D. Kontaxakis, A. Parmigiani, D. Lagrava, F. Brogi, M. B. Belgacem, Y. Thorimbert, S. Leclaire, S. Li, et al., *Computers & Mathematics with Applications* **81**, 334 (2021), ISSN 0898-1221, development and Application of Open-source Software for Problems with Numerical PDEs.
- ¹⁴⁵P. Coveney, R. Highfield, and V. Ramakrishnan, *Virtual You: How Building Your Digital Twin Will Revolutionize Medicine and Change Your Life* (Princeton University Press, 2023).